




# The role of defects in the structural and photocatalytic properties of Mg/B co-doped ZnO nanoparticles

K. Senturk<sup>1</sup>, B. Yalcin<sup>2</sup>, I. E. Yalcin<sup>3</sup>, M. C. Alphan<sup>4</sup>, M. S. Sengul<sup>5</sup>, C. Tav<sup>5</sup>,  
U. Yahsi<sup>5</sup>, and L. Arda<sup>6,\*</sup> 

<sup>1</sup>Department of Mechatronics Engineering, Istanbul Gelisim University, 34310 Istanbul, Türkiye

<sup>2</sup>Department of Medical Laboratory Techniques, Bahcesehir University, 34353 Istanbul, Türkiye

<sup>3</sup>Department of Civil Engineering, Bahcesehir University, 34353 Istanbul, Türkiye

<sup>4</sup>Department of Electric Electronic Engineering, Bahcesehir University, 34353 Istanbul, Türkiye

<sup>5</sup>Faculty of Science, Department of Physics, Marmara University, 34722 Istanbul, Türkiye

<sup>6</sup>Department of Mechatronics Engineering, Bahcesehir University, 34353 Istanbul, Türkiye

**Received:** 31 December 2022

**Accepted:** 3 March 2023

**Published online:**

29 March 2023

© The Author(s), under exclusive licence to Springer Science+Business Media, LLC, part of Springer Nature 2023

## ABSTRACT

Mg/B co-doped ZnO nanoparticles were synthesized by using the sol-gel technique to investigate the role of the defects on the structural, biological and photocatalytic properties. Single phases with ZnO wurtzite hexagonal structures were observed in the X-ray diffraction measurements. Scanning electron microscopy and transmission electron microscopy were used to determine the surface, particle size, and shapes of the nanoparticles. Electron dispersive spectroscopy was used to determine the elemental compositions of the nanoparticles. Photoluminescence spectrophotometry and positron annihilation lifetime spectroscopy were used to study the defect type, density and crystal quality of Mg/B co-doped ZnO nanoparticles. A broad visible emission band (including violet-blue-orange and red emissions) was observed. The violet-blue-orange and red emissions could be attributed to the O vacancies ( $V_O$ ), interstitial Zn ( $Zn_i$ ), Zn vacancies ( $V_{Zn}$ ), and the double charged oxygen vacancy ( $V_O^{++}$ ), which were strongly dependent on the synthesis conditions and doping ratio. SEM images revealed that Mg/B-co-doped ZnO nanoparticle magnifications were dense, quasispherical, and agglomerating. The photocatalytic activities and blood compatibilities of Mg/B co-doped ZnO nanoparticles were studied by the photocatalytic degradation tests of crystal violet (CV) and hemolysis tests, respectively.

Address correspondence to E-mail: [lutfi.arda@eng.bau.edu.tr](mailto:lutfi.arda@eng.bau.edu.tr)

## 1 Introduction

Especially in the last decades of the century, research on metal oxides has attracted the increasing attention of many researchers from various fields, such as materials science, chemistry, physics, and medicine. Nanomaterials with high structural stability, improved/tuned mechanical and electrical properties, photocatalytic and antibacterial properties, and blood and tissue compatibility can be used in medical fields, magnetic hyperthermia applications, and controlled drug release, alone or as organic–inorganic nanocomposites [1, 2]. Zinc oxide (ZnO) particles are metal oxide nanostructures that are in high demand for many different applications. ZnO nanoparticles show structural and thermal stability [3] and possess enhanced electronic [4], optical [5] and semiconductor properties. The most important features that make ZnO nanostructures suitable for almost an infinite number of applications are their wide direct band gap energy (3.37 eV) [6] and high exciton binding energy (60 meV) at room temperature [7]. In addition, ZnO nanoparticles have lower toxic effects on various cell lines and show higher biocompatibility than other nanosized metal oxides [8]. The critical biological properties of ZnO nanoparticles, such as anti-inflammatory, antimicrobial, antidiabetic and anticancer properties, make them high-potential materials in terms of medicine.

Improved mechanical properties and structural stability of Mg/B co-doped ZnO under physiological conditions as well as tunable photoactivity by adjusting particle size [9] will make these nanoparticles an efficient and tough competitor toward other nanosized materials in the field. In this context, the level of photocatalytic activity of ZnO can be enhanced by using methods such as adding transition metals, using coupled semiconductors, and doping nonmetals [10]. In the study of Samanta et al., a chemical precipitation method was followed using hydroxy oxalate precursors to synthesize  $Zn_{1-x}Mg_xO$  nanoparticles with enhanced photocatalytic activity [11]. The positive effects of the presence of magnesium in the structure on the photocatalytic properties of ZnO have been tried to be improved in various studies by adding a second component to the ZnO structure together with Mg [12–15]. In these studies, synthesized nanostructures were obtained by methods such as coprecipitation and solid-state reactions. AlMgZnO films synthesized by the sol–gel method

were offered as a promising solution for CO and CO<sub>2</sub> detection in biomedical applications [16]. Another study that focused on the type of precursor zinc salts on morphology and photocatalytic properties revealed that zinc sulfate showed the strongest enhancing effect over nitrate, acetate and chloride precursors [17]. However, the main goal is to synthesize nanomaterials with the general structural properties required for the targeted application area. For example, for a nanometal oxide-based/doped material that is planned to be used in biological applications, while significant photocatalytic activity has a positive effect on the antibacterial properties of the material, reactive oxygen species, which are the source of this effect, may cause oxidative stress and related damage to living tissue. Since the US Food and Drug Administration approved ZnO nanoparticles as Generally, Recognized as Safe (GRAS) materials for human health, they have the potential to be used in drug delivery applications [9, 18]. In a related literature study, heparin-loaded ZnO nanoparticles were embedded in a hydrogel matrix and investigated for their in vivo and in vitro properties as wound dressings [19]. In this study, it was emphasized that ZnO improves the physical and mechanical properties of wound dressings designed for acute wounds, does not show toxic effects on skin cells, and shortens the wound healing process. MgZnO nanoparticles were found to have the ability to create interactions with biological molecules such as RNA and proteins [20]. Mn-, iron (Fe)-, nickel (Ni)-, and cobalt (Co)-doped ZnO nanoparticles were also investigated, and valuable preclinical data were published for their antiviral and anticancer activities [21]. Based on this, it was predicted that Mg and B co-doped ZnO could also result in improved biocompatibility properties. However, nanosized particles may change the physiology and integrity of cell membranes and may cause necrosis [22, 23]. At this point, the necessity of blood compatibility tests of a new synthetic material that is about to be presented to the literature is undoubted. According to ISO/TR 7406, materials causing less than 5% hemolysis are considered safe for human use. Tanweer et al. (2022) investigated the material properties as well as the biocompatibility of restorative composite materials for dental use [24]. The researchers emphasized that 1–2.5% Mg doped into the ZnO nanostructure causes hemolysis below 5% at the end of the incubation period under physiological conditions; therefore, it

does not have a toxic effect on human erythrocytes. Moreover, in a study investigating the potential of hydrothermally synthesized ZnO and neodymium (Nd)-doped (4%) ZnO nanostructures for therapeutic applications, it was stated that pure ZnO nanoparticles were nonhemolytic at concentrations lower than 5 mg/ml. In the same study, it was also stated that ZnO nanoparticles were better in terms of blood compatibility than NdZnO nanostructures [25].

Another feature of metal oxide nanoparticles that has been extensively researched is their ability to degrade organic molecules such as textile dyes, antibiotics, and pesticides through photocatalytic reactions [26–28]. In particular, waste from the textile and dye industries plays an important role in increasing contamination hazards, which can result in serious health problems for human beings and damage to the environment [29]. Nanomaterials and methods that can reduce or remove organic or inorganic pollutants from the environment have recently gained great interest. The methods that have become quite popular and economic for the degradation and mineralization of organic pollutants in aqueous matrices are advanced oxidation processes (AOPs). These processes are mostly based on the generation of highly reactive species but are quick and act non-selectively in nature [30]. The ability to degrade hazardous organic wastes in an aqueous medium using natural sunlight and UV irradiation is an important property of nanocomposites. Therefore, the photocatalysts that take place in employing these processes (AOPs) are under the investigation of researchers and are extensively studied [31, 32]. AOPs can be used for the complete degradation of organic contaminants. The photocatalytic process is one of the developing AOPs. Photocatalysts that play an important role in these processes and are mostly studied can be summarized as ZnO, TiO<sub>2</sub>, and CdS. Even though TiO<sub>2</sub> is considered the best photocatalyst among the semiconductors mentioned above, its uneconomical widespread use is a very important disadvantage [33]. High redox potential and superior chemical and physical stability are the advantages of ZnO compared with other semiconductors. Especially when compared with TiO<sub>2</sub>, ZnO can absorb and utilize larger fractions of the solar spectrum [34]. ZnO is not only a photocatalyst but also an antibacterial agent. A doping element can change the level of photocatalytic activity of nanomaterials [35]. ZnO's

ability to degrade various pollutants is because of its high photosensitivity [36].

The doping process causes some structural, optical, magnetic, and electrical changes in the properties of ZnO [37–41]. By doping metaloxides, properties such as transmittance, refractive index, optical band gap, conductivity, etc., can be tuned [42]. Due to their excellent optical and electrical properties and chemical stability, doped ZnO nanomaterials have been used in solar cells, smart windows, and light-emitting diode technologies [43]. In the studies related to B-doped ZnO nanoparticles, they found that the sensitivity of the films to some gases such as CO increases as a result of grain size decrease and increase in roughness. The sensitivity of the film is directly proportional to the concentration of B [44]. The optical band gap of B-doped ZnO films gradually decreases with B concentration [45]. The carrier concentration of B-doped ZnO is lower than that of ZnO doped with Al [38]. Additionally, ZnO doped with B shows improved semiconductor properties as a result of a decrease in wurtzite crystallite size and narrowed Eg value together with enhanced photocatalytic activity [46]. The surface morphology of ZnO is also affected by the doping concentration of B [47]. The increase in B concentration results in an increase in carrier concentration, a decrease in Hall mobility and a decrease in electrical resistivity at room temperature. These results show that B atoms act as electron donors in ZnO, causing an increase in electrical conductivity and a decrease in transparency [48]. Since the transmittance decreases with increasing B concentration, the refraction index is also affected, and it increases with increasing B concentration [49].

Mg doping on ZnO causes an increase in the bandgap value. Additionally, a decrease in crystalline size with an increase in the doping ratio of Mg and an increase in antibacterial activity are observed [50]. This process can result in the enhancement of the optical and electrical properties of ZnO [51]. An increase in Mg concentration can cause agglomeration in the sample. Doping with Mg, ZnO shows ferromagnetic properties when pure ZnO is paramagnetic at room temperature [52]. By changing the Mg concentration, tuning of the bandgap of ZnO from 3.3 to 7.8 eV is possible [34]. It is among the important points emphasized by the studies presented in the literature that the structural and material properties of metal oxide nanoparticles are

strongly affected by the type of precursor, solvent type, whether calcination is applied and calcination temperature [53–55]. In one of the limited number of studies examining ZnO nanostructures with Mg and B doped together, MgBZnO nanoparticles were synthesized in organic solvent by a one-pot method [56]. In a related study, nanoparticle synthesis was initiated with acetylacetonate precursors and proceeded in the presence of oleylamine (surfactant), oleic acid (sol stabilizer) and octadecene (solvent). In that study presented in the literature, the researchers reported that the codoping of Mg and B preserves the wurtzite structure, that increasing the amount of B increases the dislocation density, and that increasing the amount of Mg promotes the microcrystalline structure.

In this study, the physical effects of Mg/B codoping into ZnO nanoparticles were investigated. Although there are many studies investigating MgZnO and boron-doped ZnO structures, only a few studies have been reported in which these two elements are used together as dopants. Additionally, our literature search shows that ZnO and its derivatives are promising materials, especially for medical applications. However, the interactions between the structural components in nanosized materials and the material-living tissue/blood interactions are still an incomplete issue. Thus, there are still open questions on whether these nanomaterials have potential in medical applications and in *in vivo* applications or show adverse effects on living cells. After a comprehensive literature review, it was predicted that the use of boron and magnesium together as dopants may have possible improving effects on the structural properties as well as the photocatalytic and biocompatibility properties of the material. As a result, this study investigates and reports the effect of defects on the structural and photocatalytic properties of ZnO after co-doping with Mg and B. Thus, this study will also contribute to understanding how these novel B/Mg co-doped ZnO nanoparticles affect the integrity of erythrocytes. The collected data provided valuable data on the biocompatibility of the ZnMgBO structure and could be adapted to other cell types in living tissues in future studies.

## 2 Materials and methods

### 2.1 Nanoparticle synthesis

As precursor materials, we used zinc acetate dihydrate ( $\text{Zn}(\text{CH}_3\text{COO})_2 \cdot 2\text{H}_2\text{O}$ , Merck), boric acid ( $(\text{H}_3\text{BO}_3)$  Merck), and magnesium acetate tetrahydrate ( $\text{Mg}(\text{CH}_3\text{COO})_2 \cdot 4\text{H}_2\text{O}$ , Alfa Aesar) without further purification.

Moreover, we also used HPLC grade methanol (Merck) to arrange clear homogenous solutions and added monoethanolamine (Merck) as a sol stabilizer. The concentrations of precursor solutions ( $\text{Zn}(\text{CH}_3\text{COO})_2 \cdot 2\text{H}_2\text{O}$  and  $\text{Mg}(\text{CH}_3\text{COO})_2 \cdot 4\text{H}_2\text{O}$ ) were prepared to be 0.25 mol/L and mixed with a magnetic stirrer at room temperature overnight. It was dried under magnetic stirring in an ambient atmosphere to obtain the gel phase.

$\text{Zn}_{0.98-x}\text{Mg}_{0.02}\text{B}_x\text{O}$  NPs ( $x = 0.0\text{--}0.05$  with a 0.01 increment) were synthesized by using the sol-gel method (Fig. 1), which is described in detail below. After the amounts of materials calculated are weighed with sensitive scales, they are transferred into a 50 ml beaker. Additions are made according to the rates in %. First, 40 ml of methanol (99.8% pure) was added to each beaker, and then 600  $\mu\text{L}$  of monoethanolamine was added. The magnetic stirrer fish was placed into the beaker, and its open side was covered with stretch or parafilm. This solution was mixed at 300 rpm for at least 5 h in the mixer without heating. Then, the solvent is evaporated, leaving the mouth open.

In our studies, the mixing period is 24 h. After that, the beaker was placed in an ash oven, as shown in Fig. 2, and preheated at 400 °C for 10 min under air to burn the organic material and evaporate the remaining solvent. As the last step, to obtain the preferred phases and physical possessions, we applied 60 °C temperature for each sample separately. After the nanoparticles were synthesized, their structural, photocatalytic, antibacterial activities, and blood compatibility tests were conducted.

### 2.2 Structural analysis

The X-ray diffraction technique for synthesized B/Mg co-doped ZnO NPs with a Cu  $K\alpha$  radiation source in the scan range of  $10^\circ \leq 2\theta \leq 90^\circ$  with a scan speed of  $3^\circ/\text{min}$  was used to provide the structural phase definition by using a Rigaku diffractometer.



**Fig. 1** Flowchart for  $Zn_{0.98-x}Mg_{0.02}B_xO$  polycrystalline nanopowder synthesis

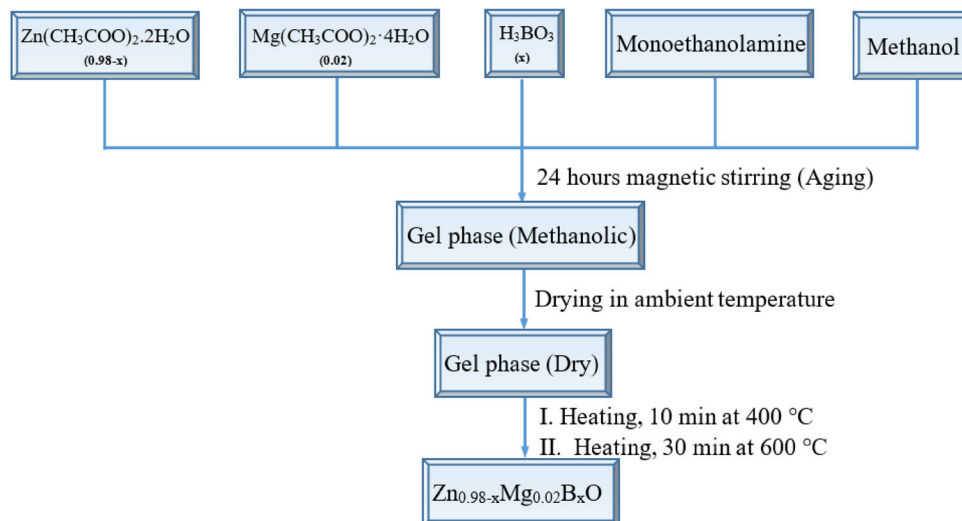


**Fig. 2** The ash used for the synthesis of  $Zn_{0.98-x}Mg_{0.02}B_xO$  nanoparticles

The surface morphology images of the Mg/B co-doped ZnO nanoparticles were determined by using a scanning electron microscope (SEM) of the JEOL, JSM-5910LV model and Transmission Electron Microscope. An Agilent Cary Eclipse Fluorescence Spectrophotometer was used to determine photoluminescence properties.

### 2.3 Photocatalytic activity measurements

The photocatalytic properties of magnesium and boron co-doped ZnO NPs were investigated by pursuing the degradation of a model dye (crystal violet—CV) in an aqueous solution at 254 nm irradiation. The concentrations of  $Zn_{0.98-x}Mg_{0.02}B_xO$  dispersions and CV in aqueous solution were adjusted to 1.0 mg/ml and  $2.5 \times 10^{-6}$  M, respectively. The photocatalytic property measurements were conducted using a

simple setup comprised of a Teflon-coated magnetic stirring bar and a borosilicate beaker containing 1.0 mg/ml of the photocatalyst ( $Zn_{0.98-x}Mg_{0.02}B_xO$ ) in a 50 mL aqueous solution of CV.  $Zn_{0.98-x}Mg_{0.02}B_xO$  dispersions were irradiated under continuous stirring with a couple of 254 nm UV lamps (45 W each), which were placed vertically on the reaction vessels at a distance of 40 cm. At specific time intervals, 1.5 ml aliquots were taken and centrifuged at 4000 rpm for 3 min to precipitate suspended nanoparticles. Supernatants were analyzed using a Shimadzu UV mini UV–visible spectrophotometer at 591 nm.

Changes in the concentration of CV were calculated from the spectrophotometric data. Distilled water was used as a reference for all samples.

The photocatalytic degradation rate constants of  $Zn_{0.98-x}Mg_{0.02}B_xO$  nanoparticles were calculated by first-order kinetic Eq. 1;

$$\ln \left( \frac{A_0}{A} \right) = kt \tag{1}$$

where  $A_0$  and  $A$  are the absorbance values of the supernatant equilibrium conditions ( $t = 0$ ) and at a given time ( $t$ ), respectively, and  $k$  is the first-order photocatalytic degradation rate constant.

### 2.4 Hemolytic activity tests

The hemolytic activities of  $Zn_{0.98-x}Mg_{0.02}B_xO$  nanoparticles were measured as described previously [57]. Whole blood samples provided by healthy donors were first anticoagulated using 0.108 mM trisodium citrate solution before dilution with Ca-

and Mg-free phosphate buffer solution (PBS). Then, blood samples were centrifuged at 4000 rpm for 5 min for the separation of erythrocytes from blood plasma. After the supernatant was decanted, erythrocytes were diluted to 50 ml using PBS. In each test, 1.0 ml of erythrocyte stock solution was incubated with two different concentrations (1.0 mg/ml and 5.0 mg/ml) of  $Zn_{0.98-x}Mg_{0.02}B_xO$  nanoparticles.

Distilled water and PBS were used in positive and negative control tests corresponding to 100% and 0% hemolysis of all erythrocytes, respectively. After 3 h of incubation at 37 °C, the samples were centrifuged, and the absorption spectra of the supernatant were recorded from 200 to 800 nm to investigate hemoglobin release from erythrocytes due to destruction of the cell membrane. The average of two separate experiments was used to evaluate the hemolytic potential of each sample.

Percent hemolysis values were calculated using the equation given below. The results were expressed as the percentage of hemolytic activity (Eq. 2).

$$\% \text{Hemolysis} = \frac{ABS_{\text{test sample}} - ABS_{\text{negative control}}}{ABS_{\text{positive sample}} - ABS_{\text{negative control}}} \times 100 \quad (2)$$

## 2.5 Positron annihilation lifetime spectroscopy

Positron annihilation lifetime spectroscopy (PALS) is a nondestructive spectroscopy technique that allows the study of various phenomena and material properties at the atomic scale. The key point of the PALS system is solely to measure the time interval between the start signal as 1274 keV prompt gamma and the stop signal as 511 keV annihilation gamma. The employed system for this purpose is the fast-fast coincidence system. The positron source we used was prepared by evaporating approximately 30  $\mu\text{Ci}$  of  $^{22}\text{NaCl}$  aqueous solution on a thin aluminum foil (5  $\mu\text{m}$  thick). We placed the source between two film samples of at least 2 mm thickness.

Two detectors with plastic scintillators (BC422, Saint-Gobain Crystals, Ohio, USA) mounted on the PMTs (photon multiplier tubes) (PMT R2059, Hamamatsu Photonics Deutschland GmbH Herrsching, Germany) with PMT Bases (265A, Ortec AMETEK GmbH, Meerbusch, Germany) were used to detect the gammas. Two constant fractional differential discriminators (CFDD 583B, Ortec AMETEK

GmbH, Meerbusch, Germany) were used for window settings and timing signals of 1274 keV and 511 keV gammas. A time-to-amplitude converter (TAC 566, Ortec AMETEK GmbH, Meerbusch, Germany) converts the time difference from both CFDDs to signal heights and then fed in a multichannel analyzer (ASPEC 927 MCA, Ortec AMETEK GmbH, Meerbusch, Germany). Spectroscopic data from MCA were analyzed to obtain lifetimes and their intensities. For such work, we need one million data points for good statistics to extract the lifetime parameters.

In general, there are three lifetime components with states: the short-lived component para-Ps (p-Ps) lifetime ( $\tau_1$ ) and its intensity ( $I_1$ ), direct annihilation lifetime ( $\tau_2$ ) and its intensity ( $I_2$ ), and the longest-lived component ortho-Ps (o-Ps) lifetime ( $\tau_3$ ) and its intensity ( $I_3$ ). We employed the program LT9.2 [58, 59] to obtain these values from the analysis of the spectra. The o-Ps lifetime can be used to compute the free volume size. O-Ps is assumed to be localized in an infinite spherical potential well of radius  $R$ . Tao-Eldrup had a model using the overlapping integration of the Ps wave function in a surrounding electron layer of a thickness  $\delta R = R_0 - R$  in the spherical potential well as

$$\frac{1}{\tau_0} = 2 \left( 1 - \frac{R}{R_0} + \frac{1}{2\pi} \sin \frac{2\pi R}{R_0} \right) \quad (3)$$

where  $\delta R = 0.1656$  nm is an experimentally obtained value [59–62]. The hole-free volume ( $v_f$ ) can then be calculated as follows:

$$v_f(\tau_3) = \frac{4}{3} \pi R^3 \quad (4)$$

[59, 63, 64] Kobayashi et al. (1989), Yu et al. (1994), and Schrader (2003) suggested that the free volume fraction ( $f_{v_f}$ ) is linearly related to the intensity and free volume by

$$f_{v_f} = A I_3 v_f(\tau_3) \quad (5)$$

where the constant  $A$  typically depends on material-related properties such as the positronium formation probability and the local electron density. In the literature [59, 63], the value of  $A$  is given by  $0.0018 \text{ \AA}^3$ , and we employed it to show at least its trend as a tool of the free volume fraction.

### 3 Results and discussion

#### 3.1 Structural analysis

Preparation technique and defects of the  $Zn_{0.98-x}Mg_{0.02}B_xO$  ( $x = 0.00-0.05$ ) NPs effect on the structural, photocatalytic, and hemolytic properties. In Fig. 3, X-ray diffraction (XRD) applying the Rietveld refinement method was performed in the range of  $10^\circ \leq 2\theta \leq 80^\circ$  to display the crystal structure properties and the existing phases of the Mg/B co-doped ZnO NPs. The XRD patterns of Mg/B co-doped ZnO NPs show all sample peak positions, which is in good agreement with standard JCPDS files (JCPDS Card no. 36-1451) for ZnO, which indicates the hexagonal structure with the space group of P63mc, as shown in Fig. 3a.

As shown in Fig. 3a, a single ZnO phase was obtained for all samples. More comprehensive research was conducted with Reitveld analysis, and the obtained results were compared. According to the Rietveld analysis results, B/Mg co-doped ZnO nanoparticles exhibited a ZnO phase without any secondary phase, as shown in Fig. 3b. This is due to the smaller ionic radii of  $B^{+3}$  and  $Mg^{+2}$  (0.23 Å and 0.57 Å, respectively) compared to  $Zn^{+2}$  (0.74 Å). B

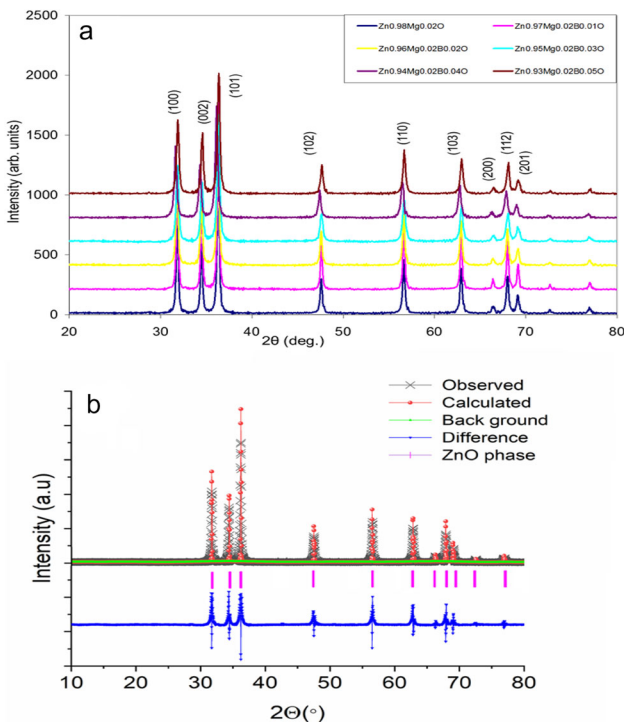


**Fig. 3** a XRD patterns of  $Zn_{0.98-x}Mg_{0.02}B_xO$  ( $x = 0.00-0.05$ ) nanoparticles and b Rietveld analysis of  $Zn_{0.93}Mg_{0.02}B_{0.05}O$

and Mg can be replaced with Zn. The concentration-dependent lattice parameters, particle sizes, atomic packing factor ( $c/a$ ), microstrain, stress, dislocation density, cell volume, and bond length were computed and depicted in Tables 1 and 2 by using XRD analysis of Mg/B co-doped ZnO NPs. How these parameters were calculated is given below. Moreover, detailed evaluations of these parameters can be found in references [65, 66].

The crystal structure and supercell of  $Zn_{0.97}Mg_{0.02}B_{0.01}O$  nanoparticles are shown in Fig. 4. The random Mg(2%)/B(1%)-doped ZnO crystal structure and supercell (Fig. 4) were visualized with the VESTA visualization package using the experimentally obtained parameters, depicted in Tables 1 and 2.

The Debye-Sherrer Eq. 6 was used to calculate the average particle sizes ( $D$ ):

$$D = \frac{K\lambda}{\beta \cos\theta} \tag{6}$$

where  $\theta$  is the angle of Bragg diffraction and  $\beta$  is the intensity at the full width at half-maximum (FWHM). The X-ray wavelength  $\lambda$  is 0.15406 nm, and  $K$  is 0.9. The calculated average nanoparticle sizes are shown in Table 1. Lattice parameters ( $a$ ) and ( $c$ ) with data from the XRD diffraction pattern were calculated using Eq.

$$\frac{1}{d_{hkl}^2} = \frac{4}{3} \left( \frac{h^2 + hk + k^2}{a^2} \right) + \frac{l^2}{c^2} \tag{7}$$

The graph of lattice parameters  $a$  and  $c$  versus B concentration is plotted in Fig. 5 for  $Zn_{0.98-x}Mg_{0.02}B_xO$  NPs.

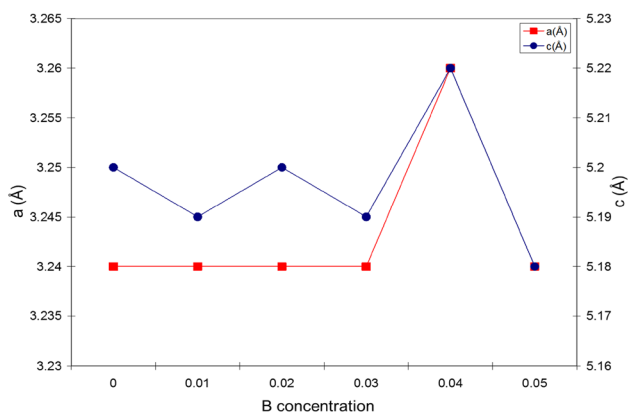
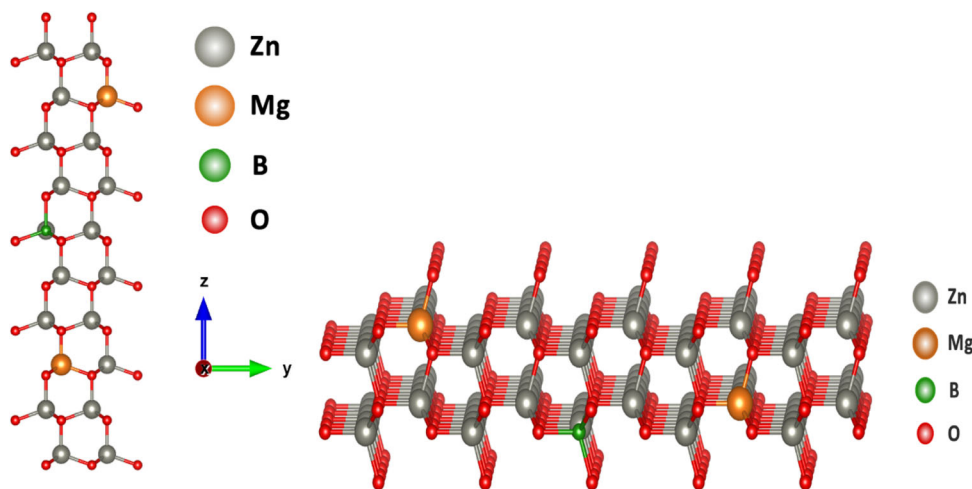
Equation 8 was used to calculate the unit cell volume ( $V$ ) of the Mg/B co-doped ZnO NPs

**Table 1** The average particle sizes  $D$ , lattice parameters  $a$  and  $c$ , atomic packing factor ( $c/a$ ) and cell volume of  $Zn_{0.98-x}Mg_{0.02}B_xO$  ( $x = 0.00-0.05$ ) nanoparticles

| Sample Name                   | $D$ (nm) | $a$ (Å) | $c$ (Å) | $c/a$ | Volume(Å <sup>3</sup> ) |
|-------------------------------|----------|---------|---------|-------|-------------------------|
| $Zn_{0.98}Mg_{0.02}O$         | 28.44    | 3.24    | 5.20    | 1.603 | 47.27                   |
| $Zn_{0.97}Mg_{0.02}B_{0.01}O$ | 32.79    | 3.24    | 5.19    | 1.601 | 47.18                   |
| $Zn_{0.96}Mg_{0.02}B_{0.02}O$ | 27.41    | 3.24    | 5.20    | 1.601 | 47.27                   |
| $Zn_{0.95}Mg_{0.02}B_{0.03}O$ | 24.87    | 3.24    | 5.19    | 1.601 | 47.18                   |
| $Zn_{0.94}Mg_{0.02}B_{0.04}O$ | 24.59    | 3.26    | 5.22    | 1.599 | 48.04                   |
| $Zn_{0.93}Mg_{0.02}B_{0.05}O$ | 23.89    | 3.24    | 5.18    | 1.600 | 47.09                   |

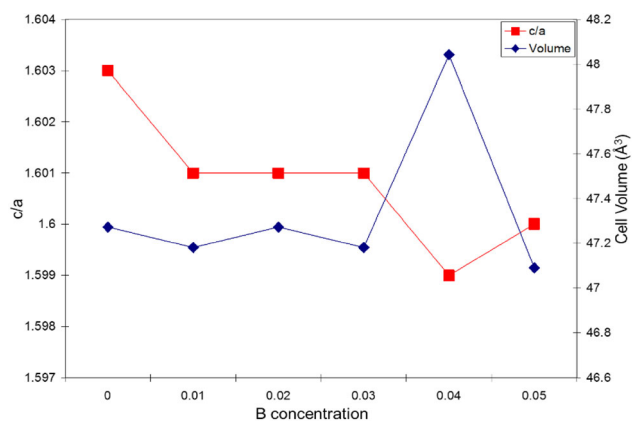
**Table 2** The dislocation density ( $\delta$ ), the locality of the atoms and their displacement ( $u$ ), bond length ( $L$ ), microstrain ( $\epsilon$ ), and stress ( $\sigma$ ) of  $\text{Zn}_{0.98-x}\text{Mg}_{0.02}\text{B}_x\text{O}$  ( $x = 0.00\text{--}0.05$ ) nanoparticles

| Sample Name   | Microstrain ( $\epsilon$ ) | Stress ( $\sigma$ ) | Dislocation density ( $\delta$ ) | Displacement ( $u$ ) | Bond length ( $L$ ) |
|---|----------------------------|---------------------|----------------------------------|----------------------|---------------------|
| $\text{Zn}_{0.98}\text{Mg}_{0.02}\text{O}$                | 0.00122                    | − 23.7229           | 0.00124                          | 0.37941              | 1.97292             |
| $\text{Zn}_{0.97}\text{Mg}_{0.02}\text{B}_{0.01}\text{O}$ | 0.00106                    | − 23.2840           | 0.00093                          | 0.37991              | 1.97172             |
| $\text{Zn}_{0.96}\text{Mg}_{0.02}\text{B}_{0.02}\text{O}$ | 0.00126                    | − 21.8882           | 0.00133                          | 0.37941              | 1.97292             |
| $\text{Zn}_{0.95}\text{Mg}_{0.02}\text{B}_{0.03}\text{O}$ | 0.00139                    | − 22.6979           | 0.00162                          | 0.37991              | 1.97172             |
| $\text{Zn}_{0.94}\text{Mg}_{0.02}\text{B}_{0.04}\text{O}$ | 0.00141                    | − 24.7126           | 0.00165                          | 0.38001              | 1.98365             |
| $\text{Zn}_{0.93}\text{Mg}_{0.02}\text{B}_{0.05}\text{O}$ | 0.00145                    | − 23.8116           | 0.00175                          | 0.38041              | 1.97052             |

**Fig. 4** Representation of crystal structure and supercell: Mg(2%)/B(1%) ions were replaced to host Zn using the VESTA visualization package**Fig. 5** B concentration-dependent a and c lattice parameters for  $\text{Zn}_{0.98-x}\text{Mg}_{0.02}\text{B}_x\text{O}$  nanoparticles

$$V = 0.866a^2c \quad (8)$$

The graph of  $c/a$  and cell volume versus B concentration is plotted in Fig. 6 for  $\text{Zn}_{0.98-x}\text{Mg}_{0.02}\text{B}_x\text{O}$  NPs. The  $c/a$  values were between 1.599 and 1.603, as shown in Fig. 6 and Table 1.  $c/a = 1.633$  for the ideal ZnO wurtzite structure. Considering the obtained

**Fig. 6** B concentration-dependent  $c/a$  and cell volume for  $\text{Zn}_{0.98-x}\text{Mg}_{0.02}\text{B}_x\text{O}$  nanoparticles

values, it was seen that  $c/a$  decreased with B concentration and was smaller than the ideal wurtzite structure. The smallest  $c/a$  ratio was observed at  $x = 0.04$  B concentration. The bond length ( $L$ ) of the nanoparticles is calculated using Eq. 9;



$$L = \sqrt{\frac{a^2}{3} + (0.5 - u)^2c^2} \tag{9}$$

where  $a$  and  $c$  are lattice constants of Mg/B co-doped NPs and  $u$  represents the atomic position parameter.

It can be computed for the wurtzite structure as

$$u = \frac{a^2}{3c^2} + \frac{1}{4} \tag{10}$$

If  $u = a^2/3c^2 + 1/4$ , then the nearest four cation-anion pairs are equidistant and  $u = 3/8$  (0.375) for the ideal ZnO wurtzite structure. The calculated  $u$  values are greater than 0.375 and increase with B concentration. Factors affecting stress and strain in a structure might be listed as the doping element and its ratio, synthesis methods, and annealing temperature.

Thus, Eqs. 11 and 12 were used to calculate the microstrain ( $\epsilon$ ) and stress ( $\sigma$ ), respectively

$$\epsilon = \frac{1}{4} \beta_{1/2} \cos\theta \tag{11}$$

$$\sigma = -4.536 \times 10^{11} \left( \frac{c - c_0}{c_0} \right) \tag{12}$$

The calculated microstrain and stress values of  $Zn_{0.98-x}Mg_{0.02}B_xO$  NPs are listed in Fig. 7 and Table 2.

The stress ( $\sigma$ ) values of Mg/B co-doped ZnO NPs are negative and show compressive stress, as seen in Fig. 8 and Table 2. The maximum microstrain and stress were obtained at  $x = 0.03$  and  $x = 0.04$ , respectively.

The physical defects and dislocations in  $Zn_{0.98-x}Mg_{0.02}B_xO$  NPs might be caused by the existence of stresses and strain. Hence, Eq. 13 was used to calculate the number of defects in the NPs.

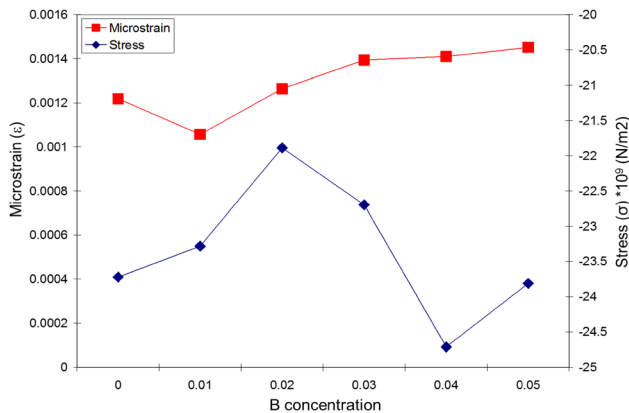


**Fig. 7** B concentration-dependent stress and microstrain for  $Zn_{0.98-x}Mg_{0.02}B_xO$  NPs

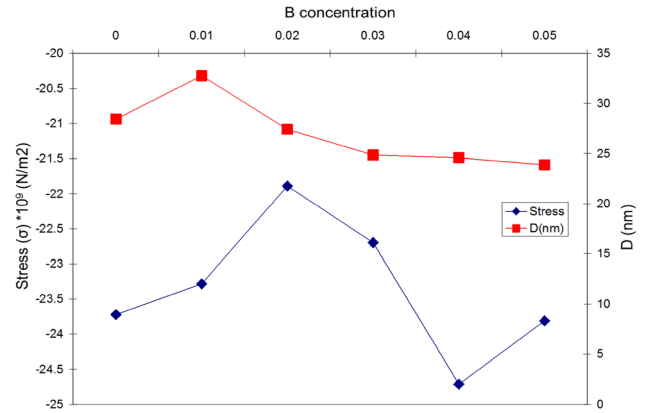


**Fig. 8** B concentration-dependent stress and microstructure for  $Zn_{0.98-x}Mg_{0.02}B_xO$  nanoparticles

$$\delta = \frac{1}{D^2} \tag{13}$$

As a result, the dislocation density ( $\delta$ ) values are shown in Table 2 and Fig. 9. When the calculated values are compared with previous studies [65, 67, 68] and the values in the literature, it is seen that Mg/B co-doped ZnO NP values are compatible and very low ( $\delta$ ), which is a good crystallinity indicator. The obtained data showed that the dislocation density increased with increasing B doping ratio, in line with the literature [56]. To better understand the crystallinity and defects of the Mg/B co-doped ZnO NPs, the photoluminescence properties of the samples were examined.

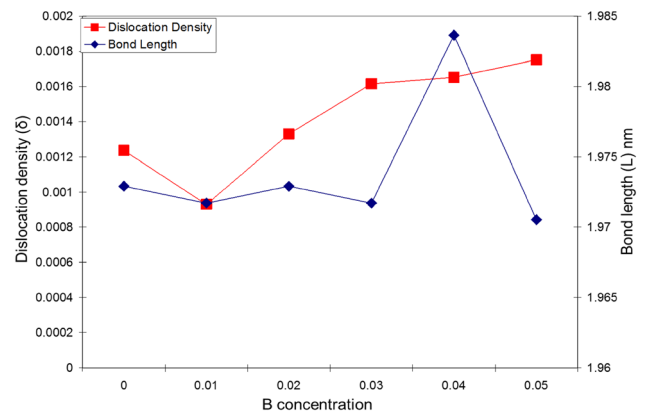


**Fig. 9** B concentration-dependent dislocation density and bond length for  $Zn_{0.98-x}Mg_{0.02}B_xO$  nanoparticles

### 3.2 Morphology of B/Mg co-doped ZnO nanoparticles

The Mg/B co-doped ZnO nanoparticles were analyzed using energy dispersive X-ray spectroscopy and mapping (SEM–FEI Quanta FEG 250) to find the concentrations of elements and their qualitative elemental constituents. The shape, nanoparticle distributions, surface mapping, and elemental composition of the  $\text{Zn}_{0.93}\text{Mg}_{0.02}\text{B}_{0.05}\text{O}$  nanoparticles annealed at 600 °C for 30 min are given in Fig. 10. Agglomeration and cone structures were observed. The size of the nanoparticles was measured to be between 42 and 62 nm. The  $\text{Zn}_{0.98-x}\text{Mg}_{0.02}\text{B}_x\text{O}$  NP compositions were examined by the EDAX spectrum. Only Zn, Mg, B, and O peaks are seen in the obtained EDAX spectra, and the absence of an extra peak indicates that we have obtained the correct structure in Fig. 10d. In addition, Zn, Mg, and B contents were found to be compatible with the synthesized NPs. Figure 11a–c shows the TEM image of the Mg/B co-doped ZnO NPs with different scales ranging from 50 to 200 nm.

In the TEM image, most of the nanoparticles appear to agglomerate. As seen from the TEM measurements, the dimensions of the nanoparticles were measured between 39.68 and 44.53 nm. Although the sizes of the nanoparticles are on the nm scale in TEM and SEM measurements, the main reason for the different values obtained is due to the agglomeration of the nanoparticles.

### 3.3 Photoluminescence

An Agilent Cary Eclipse Fluorescence Spectrophotometer was used to perform PL measurements of the Mg/B codoped ZnO nanoparticles at a wavelength of 300 nm in the range of 350 nm to 900 nm. As shown in Fig. 12, two main emission peaks were observed: a broad visible emission band and an ultraviolet (UV) emission peak. The ultraviolet (UV) emission peak is responsible for the crystallization quality, while the broad visible emission band is responsible for the intrinsic defects in ZnO.

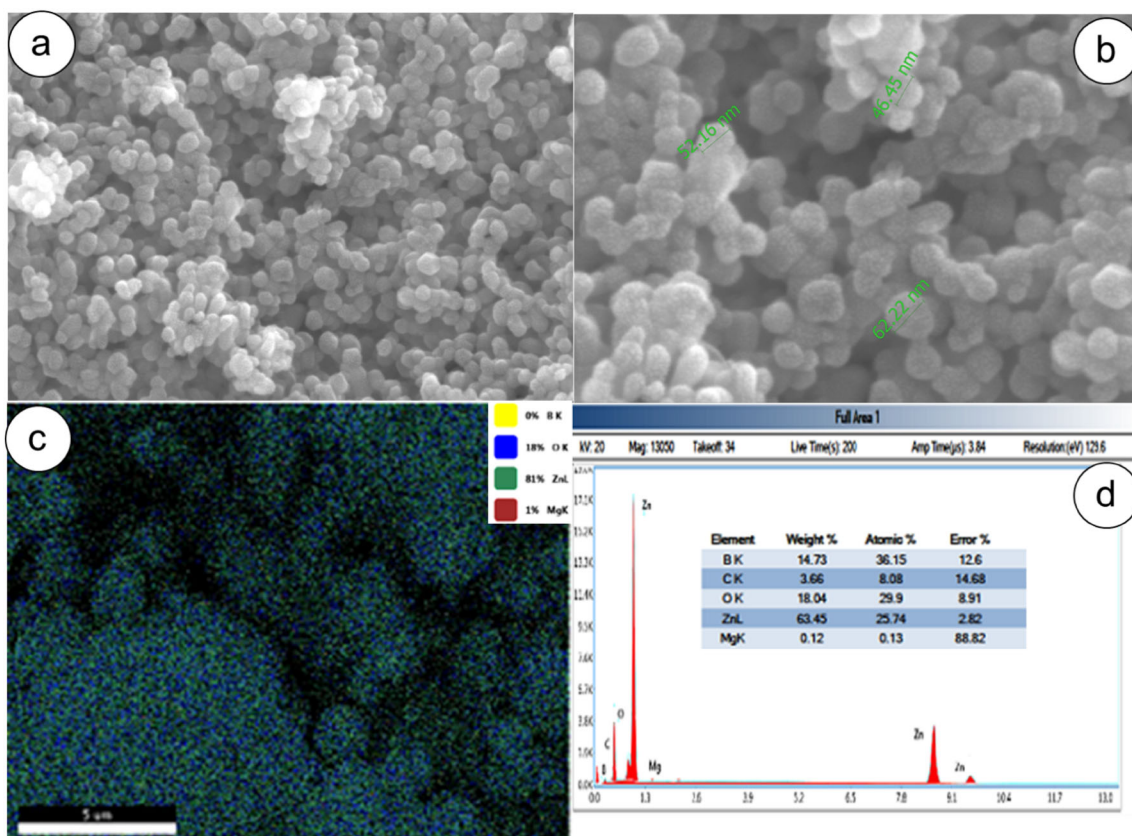


**Fig. 10** SEM images of  $\text{Zn}_{0.93}\text{Mg}_{0.02}\text{B}_{0.05}\text{O}$  composition for **a** 2  $\mu\text{m}$ , **b** 100 nm, **c** the EDX mapping images, and **d** the EDX graph of  $\text{Zn}_{0.93}\text{Mg}_{0.02}\text{B}_{0.05}\text{O}$  sample

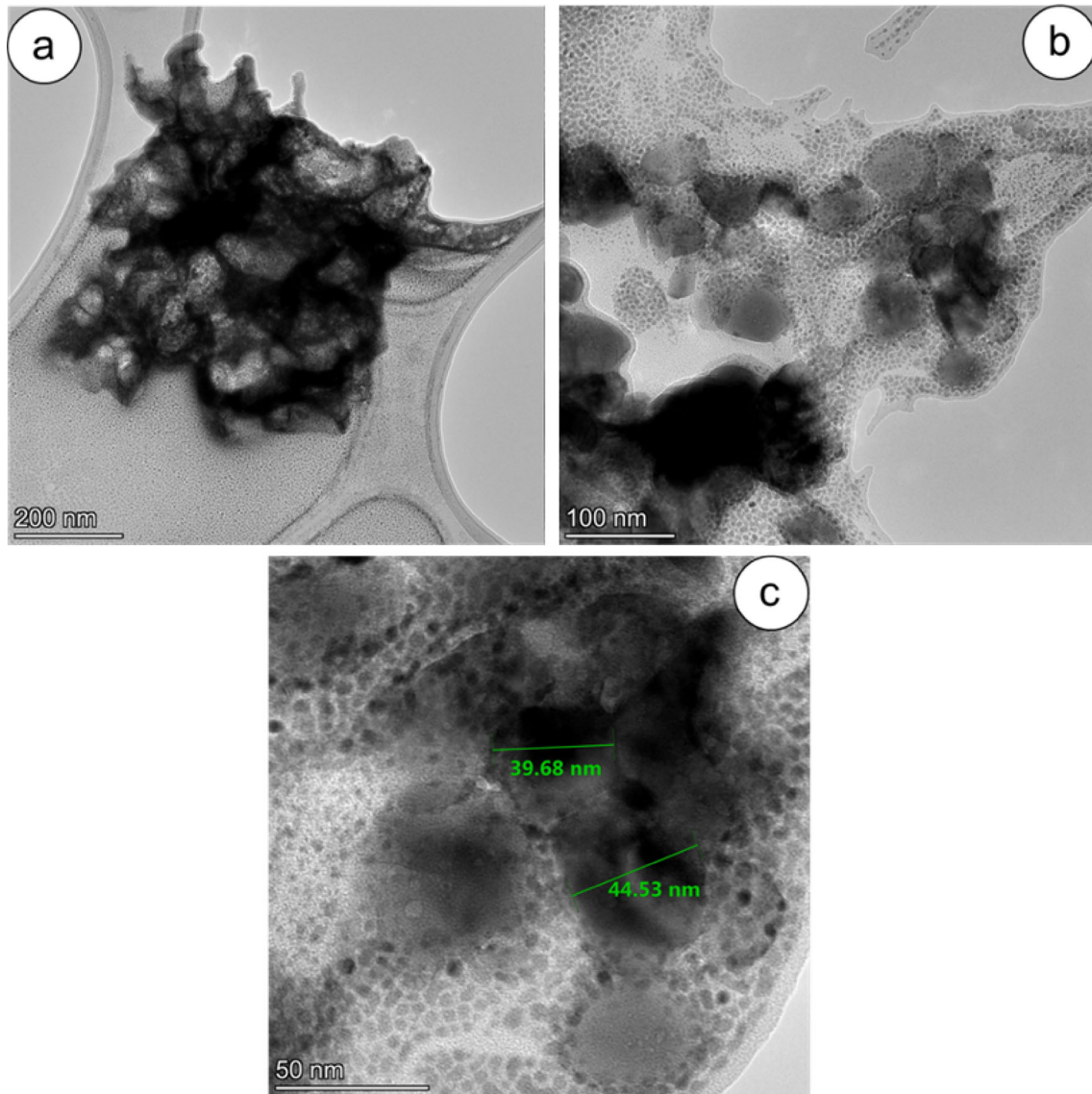


**Fig. 11** a–c TEM images of  $Zn_{0.98-x}Mg_{0.02}B_xO$  nanoparticles under different magnifications

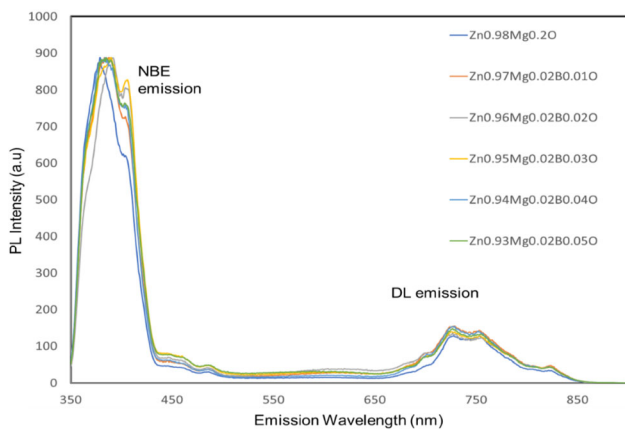


**Fig. 12** PL spectra of the B/Mg co-doped ZnO nanoparticles

A sharp transition peak corresponding to band edge emission was observed at approximately 392–395 nm for ZnO nanorods in the UV region. This emission in the UV region was generally attributed to the near band edge (NBE) transition as a common optical property of a wide bandgap of ZnO. NBE emission originated from the excitonic transitions between electrons and holes in the conduction band and the valance band, respectively [69]. Stronger ultraviolet emission is observed in ZnO with higher crystallization quality and fewer defects. Since all samples were grown at the same temperature and time, the NBE emission is almost the same height. Thus, good crystal quality Mg/B co-doped ZnO



nanoparticles could be produced at 600 °C for 30 min.

The second dominant broad emission band is a visible region, which consists of violet–blue–green–yellow–orange and red emission peaks. This visible emission is also known as the deep-level (DL) emission and is assigned to impurities or defects such as O vacancies ( $V_O$ ), Zn vacancies ( $V_{Zn}$ ), interstitial O ( $O_i$ ), interstitial Zn ( $Zn_i$ ), and substitution of O at a Zn position ( $O_{Zn}$ ). These defects are divided into two parts: interstitial zinc ( $Zn_i$ ) and oxygen vacancies ( $V_O$ ), which are donors, and interstitial zinc vacancies ( $V_{Zn}$ ), interstitial oxygen ( $O_i$ ), and oxygen antisites ( $O_{Zn}$ ), which are acceptors.

It is very difficult to obtain information about how the defects change in the visible region. Therefore, a detailed examination of the origin of the defects in the visible region is needed. Therefore, the photoluminescence spectra were subjected to Gaussian decomposition to the subpeaks according to their origination. “Fityk” software was used to obtain Gaussian decomposition. The spectrum curve model in Gaussian decomposition is determined by

$$f(\lambda) = ae^{-(\lambda-b)^2/2c^2} \quad (14)$$

As seen in Fig. 13, the eleven main Gaussian decompositions of photoluminescence spectra were plotted versus emission wavelength for B

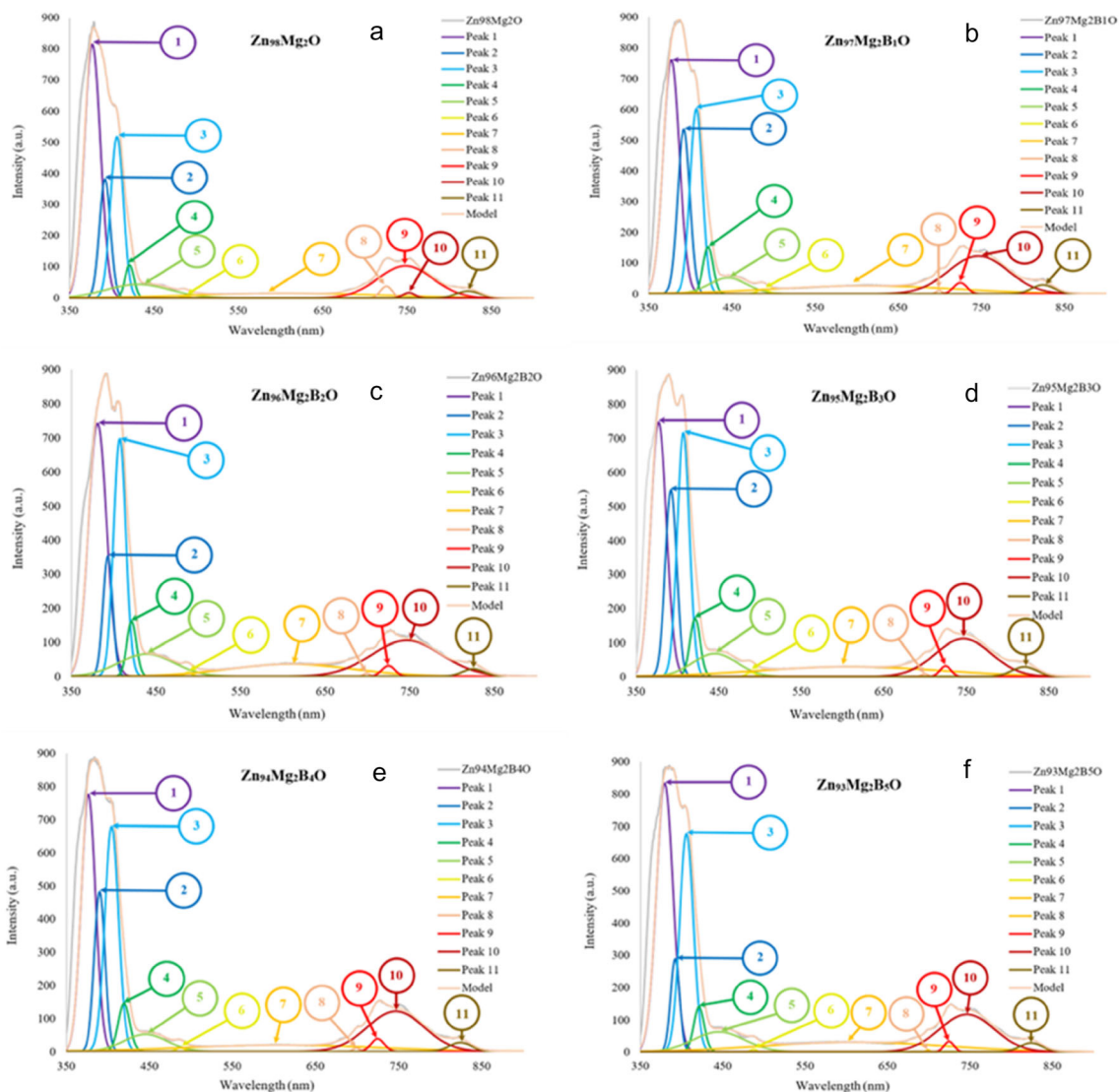


**Fig. 13** Gaussian decompositions of PL spectra of **a**  $Zn_{0.98}Mg_{0.02}O$ , **b**  $Zn_{0.97}Mg_{0.02}B_{0.01}O$ , **c**  $Zn_{0.96}Mg_{0.02}B_{0.02}O$ , **d**  $Zn_{0.95}Mg_{0.02}B_{0.03}O$ , **e**  $Zn_{0.94}Mg_{0.02}B_{0.04}O$ , and **f**  $Zn_{0.93}Mg_{0.02}B_{0.05}O$  nanoparticles



**Table 3** The peak center and area values, emission range, and origin of PL emission of the B/Mg codoped ZnO nanoparticles

| Peak label | Zn <sub>0.98</sub> Mg <sub>0.02</sub> O |         | Zn <sub>0.97</sub> Mg <sub>0.02</sub> B <sub>0.01</sub> O |         | Zn <sub>0.96</sub> Mg <sub>0.02</sub> B <sub>0.02</sub> O |         | Zn <sub>0.95</sub> Mg <sub>0.02</sub> B <sub>0.03</sub> O |         | Zn <sub>0.94</sub> Mg <sub>0.02</sub> B <sub>0.04</sub> O |         | Zn <sub>0.93</sub> Mg <sub>0.02</sub> B <sub>0.05</sub> O |         | Emission range      | Origin                           |
|------------|---|---------|---|---------|---|---------|---|---------|---|---------|---|---------|---------------------|----------------------------------|
|            | Center                                  | Height  | Center  | Height  | Center  | Height  | Center  | Height  | Center  | Height  | Center  | Height  |                     |                                  |
| Peak 1     | 376.928                                 | 815.43  | 376.928   | 760.136 | 380.829   | 741.267 | 376.928   | 746.527 | 376.54  | 775.662 | 379.527   | 832.635 | Ultraviolet         | Excitons                         |
| Peak 2     | 391.907                                 | 382.632 | 391.907   | 535.666 | 392.962   | 352.985 | 391.907   | 548.23  | 390   | 481.691 | 392.132   | 288.132 | Ultraviolet         | Excitons                         |
| Peak 3     | 406.19                                  | 519.579 | 406.89  | 601.988 | 407.042   | 696.286 | 406.89  | 715.156 | 361.953   | 391.072 | 405.927   | 676.647 | Violet              | Zn <sub>i</sub> → V <sub>B</sub> |
| Peak 4     | 421.102                                 | 105.877 | 421.102   | 151.543 | 421.104   | 159.882 | 421.102   | 169.591 | 419.466   | 144.857 | 421.102   | 139.751 | Violet              | Zn <sub>i</sub> → V <sub>B</sub> |
| Peak 5     | 431.153                                 | 43.9717 | 445.16  | 51.2479 | 438.583   | 65.7935 | 445.16  | 68.0289 | 445.16  | 52.2102 | 445.16  | 62.393  | Violet              | Zn <sub>i</sub> → V <sub>B</sub> |
| Peak 6     | 487.261                                 | 6.61535 | 487.259   | 13.9902 | 487.983   | 11.7867 | 488.953   | 12.4025 | 487.259   | 11.1177 | 487.259   | 8.04527 | Blue                | V <sub>Zn</sub>                  |
| Peak 7     | 609.366                                 | 15.0057 | 609.366   | 25.9158 | 609.366   | 35.861  | 609.366   | 29.0074 | 609.366   | 19.5666 | 609.366   | 30.5077 | Orange              | V <sub>O</sub> <sup>++</sup>     |
| Peak 8     | 725.383                                 | 37.9758 | 699.01  | 11.1178 | 699.01  | 9.24012 | 699.37  | 8.32259 | 699.01  | 11.064  | 699.01  | 6.00853 | Red                 | V <sub>O</sub>                   |
| Peak 9     | 748                                     | 102.516 | 724.613   | 35.8609 | 724.646   | 30.9048 | 724.613   | 31.0438 | 724.613   | 38.7823 | 724.613   | 32.9589 | Red                 | V <sub>O</sub>                   |
| Peak 10    | 752.194                                 | 16.8748 | 746.326   | 122.509 | 746.326   | 105.191 | 746.326   | 111.19  | 746.326   | 121.512 | 746.326   | 116.624 | Red                 | V <sub>O</sub>                   |
| Peak 11    | 822.297                                 | 22.0509 | 824.043   | 28.7775 | 824.803   | 21.6288 | 820.243   | 28.4392 | 824.043   | 27.29   | 824.043   | 27.8734 | NIR (near-infrared) | V <sub>O</sub>                   |

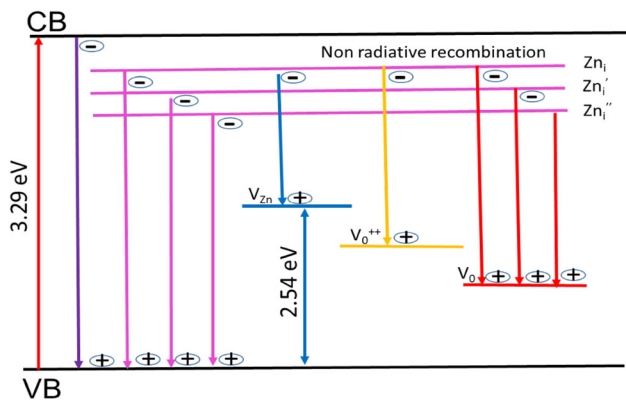


**Fig. 14** Schematic energy diagram of  $\text{Zn}_{0.98-x}\text{Mg}_{0.02}\text{B}_x\text{O}$  NPs

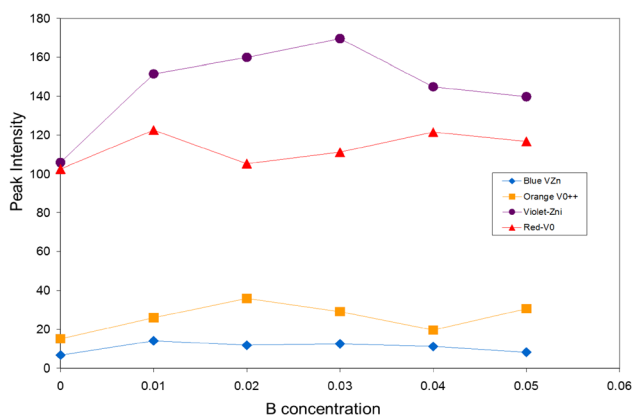


**Fig. 15** Defects as a function of B concentration ( $x$ ) of  $\text{Zn}_{0.98-x}\text{Mg}_{0.02}\text{B}_x\text{O}$  nanoparticles

concentration. The peak labels with height and position center of the different B concentrations of ZnMgO NPs are indicated in Table 3. The emissions of these peaks are (Peak 1 and Peak 2) two ultraviolet emissions, (Peak 3, Peak 4, and Peak 5) three violet emissions, (Peak 6) one blue emission, (Peak 7) one orange emission, (Peak 8, Peak 9, and Peak 10) three red emissions, and (Peak 11) one near-infrared peak, as shown in Fig. 13 and Table 3.

The emission regions shown in Table 3 could be explained as follows: ultraviolet emissions from 375 to 392 nm could be ascribed to the near band emission (NBE) of ZnO as an indication of the excitonic characteristic; violet emissions (392–450 nm) could be attributed to the transition of electrons from zinc interstitials ( $\text{Zn}_i$ ) to the valance band; blue emission (450–495 nm) might be due to zinc vacancies ( $\text{V}_{\text{Zn}}$ ), orange emissions (590–620 nm) could be due to double-charged oxygen vacancies ( $\text{V}_0^{++}$ ), and red emissions (620–690 nm) and (690–750 nm) could be

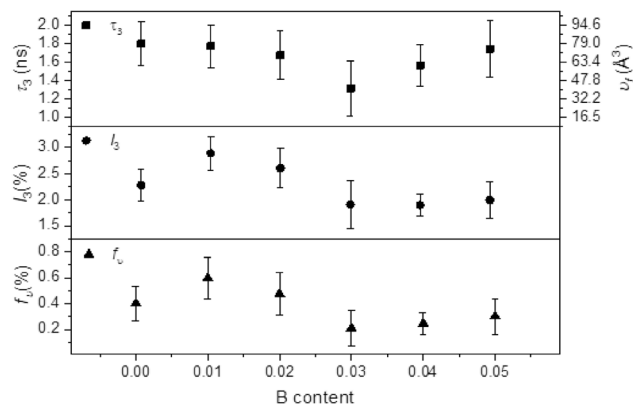


**Fig. 16** The o-Ps lifetime (with the corresponding free volume on the left axis), the o-Ps intensity and the free volume fraction versus B content

ascribed to oxygen interstitials ( $\text{O}_i$ ) and oxygen vacancies ( $\text{V}_0$ ), respectively. The near-infrared (NIR) region (750–768 nm) was related to secondary UV diffraction. Peak 11, which is NIR emission, was observed by Senol et al. [69], and it could be caused by oxygen vacancies.

The illustrative energy level diagram is shown in Fig. 14 drawings of transitions located between the valence band (VB) and conduction band (CB) guiding various emissions in the UV and visible regions according to the results of Gaussian decompositions of PL spectra.

It can be concluded that the reactions during the synthesis of  $\text{Zn}_{0.98-x}\text{Mg}_{0.02}\text{B}_x\text{O}$  NPs by the sol-gel technique cause Zn vacancies ( $\text{V}_{\text{Zn}}$ ), O vacancies ( $\text{V}_0$ ), interstitial Zn ( $\text{Zn}_i$ ), and double-charged oxygen vacancies ( $\text{V}_0^{++}$ ), as shown in Fig. 15. When the heights of the peaks given in Table 3 and Fig. 15 are examined in detail, it is seen that O vacancies ( $\text{V}_0$ ), interstitial Zn ( $\text{Zn}_i$ ), and the double-charged oxygen vacancy ( $\text{V}_0^{++}$ ) defects are dominant and showed that B/Mg-doped ZnO NPs had more donor defects. These defects (O vacancies ( $\text{V}_0$ ), interstitial Zn ( $\text{Zn}_i$ ), and the double-charged oxygen vacancy ( $\text{V}_0^{++}$ )) act as electron donors, giving rise to free electrons, and they affect the structural, luminescence, and photocatalytic properties of  $\text{Zn}_{0.98-x}\text{Mg}_{0.02}\text{B}_x\text{O}$  NPs.

### 3.4 PALS results

We took the lifetime spectra of the  $\text{Zn}_{0.98-x}\text{Mg}_{0.02}\text{B}_x\text{O}$  ( $x = 0.00$ – $0.05$ ) samples sandwiched around the positron source (on a 5  $\mu\text{m}$  Al folio) at approximately 30  $\mu\text{Ci}$  and one million counts for each spectrum.

**Table 4** PALS parameters as lifetimes ( $\tau_2$  and  $\tau_3$ ) and intensities ( $I_2$  and  $I_3$ ) with hole radius ( $R$ ) in terms of B content

| B content (%) | $\tau_2$ (ns) ( $\pm 0.047$ ) | $I_2$ (%) ( $\pm 0.8$ ) | $\tau_3$ (ns) ( $\pm 0.30$ ) | $I_3$ (%) ( $\pm 0.47$ ) | $R$ (Å) ( $\pm 0.38$ ) | $f_v$ (%) ( $\pm 0.16$ ) |
|---------------|-------------------------------|-------------------------|------------------------------|--------------------------|------------------------|--------------------------|
| 0             | 0.362                         | 82.1                    | 1.80                         | 2.28                     | 3.09                   | 0.40                     |
| 1             | 0.355                         | 78.7                    | 1.77                         | 2.89                     | 3.55                   | 0.60                     |
| 2             | 0.357                         | 81.8                    | 1.67                         | 2.61                     | 3.35                   | 0.48                     |
| 3             | 0.353                         | 86.2                    | 1.31                         | 1.91                     | 2.76                   | 0.21                     |
| 4             | 0.362                         | 84.7                    | 1.57                         | 1.90                     | 2.75                   | 0.25                     |
| 5             | 0.353                         | 85.7                    | 1.74                         | 1.99                     | 2.84                   | 0.30                     |

The intensities were normalized as  $I_1 + I_2 + I_3 = 1$

When analyzing the PALS spectrum using the LT9.2 program, we fixed the p-Ps lifetime as  $\tau_1 = 125$  ps, and we obtained a system resolution of approximately 350 ps. All the other PALS parameters, such as direct annihilation lifetime ( $\tau_2$ ) and intensity ( $I_2$ ), o-Ps lifetime ( $\tau_3$ ) and intensity ( $I_3$ ), hole-free volume radius ( $R$ ), and free volume fraction ( $f_{vf}$ ), are shown in Table 4 for all the samples. In Fig. 16, we plotted the o-Ps lifetime (left vertical axis) with the corresponding hole-free volume (right vertical axis), the o-Ps intensity ( $I_3$ ), and the free volume fraction ( $f_{vf}$ ) with respect to B contents. The o-Ps lifetime and hole-free volume decrease up to approximately 3% B content and then increase. The B contents reduce the free volume to the lowest value of  $39.2 \text{ \AA}^3$  at 0.03 B content from  $78.7 \text{ \AA}^3$  with no B content. On the other hand, the o-Ps intensity as a measure of the number of holes has a bump at low B content with the maximum at 0.01 and right after 0.03 B content, it has a very slight increase, that is, it is almost constant.

Comparing the PALS results with the structural parameters, we observe some reduction in the free volume hole size at higher B concentrations, say 0.03 and 0.04 fractions, and the lattice constants  $a$  and  $c$  and the cell volume have an increase at 0.04 B content. A reduction in the defect hole size likely has an increasing effect on the lattice parameters and the cell volume.

The sizes of the nanoparticles increase at a 0.01 fraction of the B content and then decrease abruptly but saturate just after 0.03 B fraction. This reflects similar behavior in the o-Ps intensity as a measure of the number of holes or free volume fraction in Fig. 16. This implies that the greater the increase in the sizes of the nanoparticles, the more holes or free volume produced in the nanoparticles. Particle sizes are in the range of 23.9 to 32.8 nm, while the hole sizes change from 0.266 to 0.211 nm. Therefore, we may

attribute the change in the o-Ps intensity to the change in nanoparticle sizes with the B content change. If we compare the microstrain in Fig. 7 and the dislocation density in Fig. 9 with the o-Ps intensity in Fig. 16, they behave as inversely related. The dislocation density is inversely related to the square of the particle sizes, as in Eq. 11. From the discussion between the o-Ps intensity and the particle size, we deduce that the microstrain and the dislocation density must obey the inversely related observation with the number of defects as holes calculated from the o-Ps technique.

The compressive stress values shown in Fig. 8 are related to the defect holes or dislocations so that we may correlate the free volume fraction. Therefore, comparing the respective quantities in Fig. 8 and Fig. 16, we observe that the higher the free volume fraction is, the lower the stress, and vice versa. We may interpret that the free volume in the material causes relaxation of the stresses on the structure of the lattice.

The photoluminescence spectra discussed in the previous section showed that with B/Mg-doped ZnO NPs, donor defects are produced, such as O vacancies ( $V_O$ ), interstitial Zn ( $Zn_i$ ), and the double-charged oxygen vacancy ( $V_O^{++}$ ), as shown in Fig. 15. The donor nature of these defects attracts positrons to be in positronium states. Hence,  $V_O$  and  $V_O^{++}$  vacancies are expected to be closely related to the o-Ps intensity as the number of holes increases. The interstitial Zn ( $Zn_i$ ) defects increase with B content and then decrease slightly, as shown in Fig. 15. On the other hand,  $Zn_i$  reflects an inverse relation in the o-Ps lifetime since the Zn ions likely compress the defect volume when occupying the interstitial space.

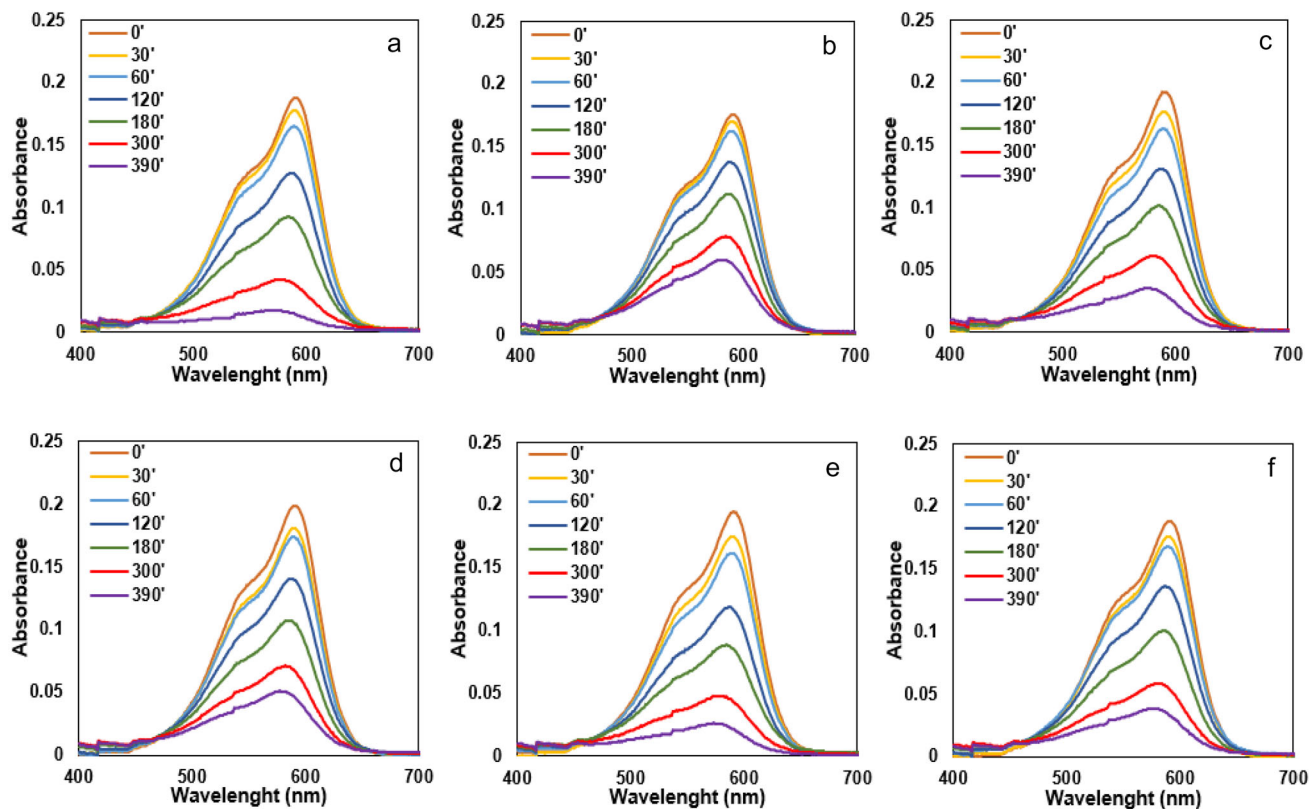


**Fig. 17** Absorption spectra of CV decolorization in the presence of **a**  $\text{Zn}_{0.98}\text{Mg}_{0.02}\text{O}$ , **b**  $\text{Zn}_{0.97}\text{Mg}_{0.02}\text{B}_{0.01}\text{O}$ , **c**  $\text{Zn}_{0.96}\text{Mg}_{0.02}\text{B}_{0.02}\text{O}$ , **d**  $\text{Zn}_{0.95}\text{Mg}_{0.02}\text{B}_{0.03}\text{O}$ , **e**  $\text{Zn}_{0.94}\text{Mg}_{0.02}\text{B}_{0.04}\text{O}$  and **f**  $\text{Zn}_{0.93}\text{Mg}_{0.02}\text{B}_{0.05}\text{O}$

### 3.5 Photocatalytic activity measurements

The photocatalytic study on  $\text{Zn}_{0.98-x}\text{Mg}_{0.02}\text{B}_x\text{O}$  nanoparticles was performed by following the degradation of an aqueous CV solution. The absorption maxima of CV molecules were found to be at 590 nm. Since photodegradation of organic pollutants such as aromatic phenolics, hydrocarbons, drugs, herbicides, or dyes predominantly occurs on the surface of photocatalytically active nanoparticles [70], CV- $\text{Zn}_{0.98-x}\text{Mg}_{0.02}\text{B}_x\text{O}$  dispersions were kept in the dark in the first 30 min to avoid photodegradation. Since a surface adsorption/desorption equilibrium is established between nanoparticle surfaces and dye molecules, the actual CV concentration was considered equal to the equilibrium concentration of CV at the beginning of irradiation [10].

UV-Vis absorption spectra of CV decolorization in the presence of  $\text{Zn}_{0.98-x}\text{Mg}_{0.02}\text{B}_x\text{O}$  nanoparticles are given in Fig. 17a-f. Decreasing absorption band intensities corresponding to 590 nm indicated the degradation of CV by both  $\text{Zn}_{0.98}\text{Mg}_{0.02}\text{O}$  and B-doped  $\text{Zn}_{0.98}\text{Mg}_{0.02}\text{O}$  nanoparticles. The intensity

of the characteristic band at the absorption maxima of CV (590 nm) significantly weakened after 390 min under the effect of 254 nm irradiation and indicated the successful photodegradation of CV. Mg-B co-doped nanoparticles ( $\text{Zn}_{0.98-x}\text{Mg}_{0.02}\text{B}_x\text{O}$ ) showed lower decolorization efficiencies than  $\text{Zn}_{0.98}\text{Mg}_{0.02}\text{O}$ . The ionic radius of  $\text{B}^{3+}$  is 0.27 Å, which is much smaller than that of  $\text{Zn}^{2+}$  ions, 0.82 Å [71]. Theoretically, as an n-type dopant,  $\text{B}^{3+}$  ions can either be dissolved in the ZnO lattice so that they substitute for  $\text{Zn}^{2+}$  ions and/or occupy the locations in interstitial regions, or boron oxide cophase can be formed. However, according to the Hume-Rothery rules, ZnO- $\text{B}_2\text{O}_3$  alloys improbably occur since the ionic radii of  $\text{Zn}^{2+}$  and the substitutional element  $\text{B}^{3+}$  are different by more than 25%. Moreover,  $\text{Zn}^{2+}$  and  $\text{B}^{3+}$  ions have different electronegativity values and valencies. Thus, the occupation of interstitial cavities of the ZnO lattice by  $\text{B}^{3+}$  ions is preferred over the formation of ZnO- $\text{B}_2\text{O}_3$  alloys. This kind of replacement disturbs the charge neutrality of the lattice and can be compensated by the formation of  $\text{Zn}^{2+}$  vacancies [72].

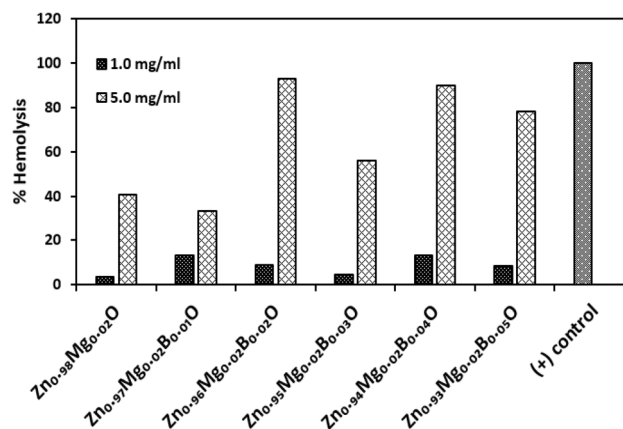


**Table 5** Photocatalytic degradation rate constants of  $Zn_{0.98-x}Mg_{0.02}B_xO$  nanoparticles and degradation percentages of CV after 390 min of irradiation

| Sample                        | %CV degradation | k (min <sup>-1</sup> ) | R <sup>2</sup> |
|-------------------------------|-----------------|------------------------|----------------|
| $Zn_{0.98}Mg_{0.02}O$         | 97.7            | 0.0068                 | 0.9634         |
| $Zn_{0.97}Mg_{0.02}B_{0.01}O$ | 77.8            | 0.0032                 | 0.9926         |
| $Zn_{0.96}Mg_{0.02}B_{0.02}O$ | 90.4            | 0.0050                 | 0.9837         |
| $Zn_{0.95}Mg_{0.02}B_{0.03}O$ | 83.0            | 0.0041                 | 0.9950         |
| $Zn_{0.94}Mg_{0.02}B_{0.04}O$ | 94.6            | 0.0060                 | 0.9893         |
| $Zn_{0.93}Mg_{0.02}B_{0.05}O$ | 88.8            | 0.0048                 | 0.9885         |

The degradation rate constants calculated by using the linear plot of  $\ln(A/A_0)$  vs time graphs corroborated the reduced photocatalytic activity of  $Zn_{0.98-x}Mg_{0.02}B_xO$  nanoparticles, which is mainly attributed to the zinc vacancies and inhomogeneous defect densities in the ZnMgO lattice (Fig. 15 and Table 5).

The photocatalytic performance of metal oxide nanoparticles depends on the surface properties, dispersity in the solution, and dopant type/concentration [73]. Boron doping generally reduced the photocatalytic performance of  $Zn_{0.98}Mg_{0.02}O$  nanoparticles. While the degradation percentages of  $Zn_{0.98-x}Mg_{0.02}B_xO$  nanoparticles were between 77.8 and 94.6% after 390 min, the corresponding value of  $Zn_{0.98}Mg_{0.02}O$  was found to be 97.7%. Varying photocatalytic performances were observed among boron-doped  $Zn_{0.98-x}Mg_{0.02}B_xO$  nanoparticles, which were mainly attributed to the lattice defects arising from the chemical properties of B. Additionally, highly “deformed” materials where the structure is disrupted by the dopant elements possess high dislocation density values [74]. Although structural defects were increased in  $Zn_{0.97}Mg_{0.02}B_{0.01}O$  compared to  $Zn_{0.98}Mg_{0.02}O$  (Fig. 15), the dislocation density was found to be quite low in  $Zn_{0.97}Mg_{0.02}B_{0.01}O$ . When the photocatalytic performances of these two samples are evaluated, it is shown that the dislocation density is more decisive on the photocatalytic properties of the samples. Thus, the low dislocation density of  $Zn_{0.97}Mg_{0.02}B_{0.01}O$  (Table 5) could be a reasonable explanation for the unexpectedly low photodegradation ability of this sample. With increasing B doping ratios (0.02–0.05), photocatalytic activities were observed depending on the  $V_O$  and  $V_O^{++}$  values.

**Fig. 18**  $Zn_{0.98-x}Mg_{0.02}B_xO$ -induced hemolysis ratios with respect to distilled water-treated cells ((+) control)

### 3.6 Blood compatibility tests

Investigation of nanomaterial interactions with model cell membranes allows a wide range of applications from diagnostics to therapeutics. Determination of the blood compatibility of nanomaterials is a well-accepted method for in vivo testing of biological properties [75]. The nanoparticle-induced hemolysis ratios of human erythrocytes exposed to two different concentrations of  $Zn_{0.98-x}Mg_{0.02}B_xO$  nanoparticles (1.0 mg/ml and 5.0 mg/ml) are given in Fig. 18. The results are given as the average of two independent experiments. Variable percentages of hemolysis were observed in the presence of  $Zn_{0.98-x}Mg_{0.02}B_xO$  nanoparticles at both concentrations. Necrosis was much greater at higher concentrations of nanoparticles for all samples, as expected.

Figure 18 also shows considerably low hemolysis ratios of  $Zn_{0.98}Mg_{0.02}O$  and  $Zn_{0.95}Mg_{0.02}B_{0.03}O$  nanoparticles at 1.0 mg/ml concentration. Hemolysis ratios that are less than 5% are regarded as safe by the standard test method for the analysis of hemolytic products of nanoparticles (ASTM E2524-08). At a 1.0 mg/ml concentration,  $Zn_{0.98}Mg_{0.02}O$  and  $Zn_{0.95}Mg_{0.02}B_{0.03}O$  nanoparticles showed 3.7% and 4.4% hemolysis, respectively, and were determined to have negligible hemolytic activity and low in vitro toxicity.

It was shown that Mg/B codoping on the ZnO matrix disrupted the layered crystalline structures of ZnO, leading to the formation of a considerable amount of lattice defects (Fig. 15). Fluctuations in both hemolysis percentages and CV photodegradation efficiencies were attributed to oxygen vacancies,

which were emphasized as affecting the ROS-producing properties of NPs [76].

## 4 Conclusion

$Zn_{0.98-x}Mg_{0.02}Cu_xO$  ( $x = 0.00-0.05$ ) NPs were synthesized by the sol-gel technique to investigate their microstructural, structural, photoluminescence, optoelectronic, photocatalytic, and biological properties for use in optoelectronic and sensor applications. By introducing B and Mg together as dopants, the intrinsic environment of ZnO changed. Rietveld analysis showed that Mg and B replace Zn substitutionally, yielding a ZnO single phase.

Defect studies of Mg/B co-doped ZnO NPs showed more donor defects. These defects (O vacancies ( $V_O$ ), interstitial Zn (Zni), and doubly charged oxygen vacancies ( $V_O^{++}$ ) act as electron donors, giving rise to free electrons, and they affect the structural, luminescence, and photocatalytic properties of  $Zn_{0.98-x}Mg_{0.02}B_xO$  NPs.

Varying photocatalytic performances were observed for  $Zn_{0.98-x}Mg_{0.02}B_xO$  nanoparticles, supporting these results and mainly attributed to defects. The degradation percentages of  $Zn_{0.98-x}Mg_{0.02}B_xO$  nanoparticles were between 77.8 and 94.6%, while the corresponding value of  $Zn_{0.98}Mg_{0.02}O$  was found to be 97.7%. In terms of blood compatibility,  $Zn_{0.95}Mg_{0.02}B_{0.03}O$  stood out among the B-doped samples and showed a very low hemolytic effect at a concentration of 1.0 mg/ml. Similar fluctuations observed in both blood compatibility assays and CV photodegradation test results indicate that the ROS generation ability of the samples has effects on both biological and photocatalytic properties. This study might guide the development of nanosized metal oxides with enhanced biocompatibility and sufficient structural properties with further research and modifications.

## Acknowledgements

The authors would like to thank the Research Funds of Bahcesehir University (Project No. BAP.2019-01.04 and BAP.2021-01.27).

## Author contributions

All authors certify that they have participated sufficiently in the work to take public responsibility for the content. Moreover, each author certifies that this work has not been and will not be submitted to other journals or published in any other publication before. KS: investigation, methodology, data curation, writing original draft, validation. BY: investigation, methodology, data curation, writing original draft, validation. IEY: investigation, methodology, data curation, validation. MCA: investigation, methodology, data curation, validation. MSS: investigation, methodology, data curation, validation. CT: investigation, methodology, data curation, validation. UY: investigation, methodology, writing original draft, data curation, validation. LA: investigation, methodology, data curation, writing original draft, validation. visualization, review, editing, supervision. On behalf of all coauthors.

## Funding

This work was supported by the Research Funds of Bahcesehir University Grant Numbers (BAP.2019-01.04) and (BAP.2021-01.27).

## Data availability

All data generated or analyzed during this study are included in this published article.

## Declarations

**Competing interest** The authors declare that they have no known competing financial interests or personal relationships that could have appeared to influence the work reported in this paper.

## References

1. P. Sadhukhan, M. Kundu, S. Chatterjee, N. Ghosh, P. Manna, J. Das, P.C. Sil, Targeted delivery of quercetin via pH-responsive zinc oxide nanoparticles for breast cancer therapy. *Mater. Sci. Eng., C* **100**, 129–140 (2019)
2. C. Muthusamy, M. Ashokkumar, A. Boopathyraja, V.V. Priya, Enhanced ferro magnetism of (Cu, Fe/Mn) dual doped ZnO nanoparticles and assessment of in vitro cytotoxicity and

- antimicrobial activity for magnetically guided immunotherapy and hyperthermia applications. *Vacuum* **205**, 111400 (2022)
3. Y. Cheng, Q.-D. Yang, J. Xiao, Q. Xue, H.-W. Li, Z. Guan, H.-L. Yip, S.-W. Tsang, Decomposition of organometal halide perovskite films on zinc oxide nanoparticles. *ACS Appl. Mater. Interfaces* **7**, 19986–19993 (2015)
  4. B. Alfakes, C. Garlisi, J. Villegas, A. Al-Hagri, S. Tamalampudi, N.S. Rajput, M. Chiesa, Enhanced photoelectrochemical performance of atomic layer deposited Hf-doped ZnO. *Surf. Coat. Technol.* **385**, 125352 (2020)
  5. A.P. Wanninayake, B.C. Church, N. Abu-Zahra, Effect of ZnO nanoparticles on the power conversion efficiency of organic photovoltaic devices synthesized with CuO nanoparticles. *AIMS Mater. Sci.* **3**(3), 927–937 (2016)
  6. A.A. Ahmad, M.H. Khazaleh, A.M. Alsaad, Q.M. Al-Bataineh, A.D. Telfah, Characterization of As-prepared PVA-PEO/ZnO-Al<sub>2</sub>O<sub>3</sub>-NPs hybrid nanocomposite thin films. *Polym. Bull.* **79**(11), 9881–9905 (2022)
  7. H. Benali, B. Hartiti, F. Lmai, A. Batan, S. Fadili, P. Thevenin, Synthesis and characterization of Mg-doped ZnO thin-films for photovoltaic applications. *Mater Today: Proc* **66**, 212–216 (2022)
  8. Y. Guo, Z. Sun, Investigating folate-conjugated combinatorial drug loaded ZnO nanoparticles for improved efficacy on nasopharyngeal carcinoma cell lines. *J. Exp. Nanosci.* **15**(1), 390–405 (2020)
  9. C. Li, H. Zhang, X. Gong, Q. Li, X. Zhao, Synthesis, characterization, and cytotoxicity assessment of N-acetyl-l-cysteine capped ZnO nanoparticles as camptothecin delivery system. *Colloids Surf. B: Biointerfaces* **174**, 476–482 (2019)
  10. R. Saravanan, S. Karthikeyan, V.K. Gupta, G. Sekaran, V. Narayanan, A.J.M.S. Stephen, Enhanced photocatalytic activity of ZnO/CuO nanocomposite for the degradation of textile dye on visible light illumination. *Mater. Sci. Eng. C* **33**, 91–98 (2013)
  11. A. Samanta, M.N. Goswami, P.K. Mahapatra, Optical properties and enhanced photocatalytic activity of Mg-doped ZnO nanoparticles. *Phys. E.* **104**, 254–260 (2018)
  12. S. Benzitouni, M. Zaabat, M.S. Aida, J. Ebothe, J. Michel, B. Boudine, T. Saidani, Morphology and photocatalytic activity of porous (In, Mg) co-doped ZnO nanoparticles. *Optik* **156**, 949–960 (2018)
  13. H.H. Kim, D.O. Kumi, K. Kim, D. Park, Y. Yi, S.H. Cho, W.K. Choi, Optimization of the electron transport in quantum dot light-emitting diodes by codoping ZnO with gallium (Ga) and magnesium (Mg). *RSC Adv.* **9**(55), 32066–32071 (2019)
  14. H. Abdullah, H. Shuwanto, D.H. Kuo, Multifunctional Ni–Mg bimetal-activated Zn (O, S) for hydrogen generation and environmental remediation with simulated solar-light irradiation. *Catal. Sci. Technol.* **11**(21), 7200–7216 (2021)
  15. E.R. Rwenyagila, I.N. Makundi, N.R. Mlyuka, M.E. Samiji, Dielectric anomalous peaks accenting ferroelectricity prospects of Li and Mg co-doped ZnO ceramics. *Results Mater.* **12**, 100226 (2021)
  16. S. Jaballah, G. Neri, H. Dahman, N. Donato, L. El Mir, Development of a ternary AlMgZnO-based conductometric sensor for carbon oxides sensing. *IEEE Trans. Instrum. Meas.* **70**, 1–7 (2021)
  17. S. Wang, P. Kuang, B. Cheng, J. Yu, C. Jiang, ZnO hierarchical microsphere for enhanced photocatalytic activity. *J. Alloy. Compd.* **741**, 622–632 (2018)
  18. S. Thomas, G. Gunasankaran, V.A. Arumugam, S. Muthukrishnan, Synthesis and characterization of zinc oxide nanoparticles of solanum nigrum and its anticancer activity via the induction of apoptosis in cervical cancer. *Biol. Trace Elem. Res.* **200**, 2684–2697 (2022)
  19. M.T. Khorasani, A. Joorabloo, H. Adeli, P.B. Milan, M. Amoupour, Enhanced antimicrobial and full-thickness wound healing efficiency of hydrogels loaded with heparinized ZnO nanoparticles: in vitro and in vivo evaluation. *Int. J. Biol. Macromol.* **166**, 200–212 (2021)
  20. A. Hoffman, X. Wu, J. Wang, A. Brodeur, R. Thomas, R. Thakkar, R.K. DeLong, Two-dimensional fluorescence difference spectroscopy of ZnO and Mg composites in the detection of physiological protein and RNA interactions. *Materials* **10**, 1430 (2017)
  21. R.K. DeLong, R. Swanson, M.C. Niederwerder, P. Khanal, S. Aryal, R. Marasini, E.N. Mathew, Zn-based physiometacomposite nanoparticles: distribution, tolerance, imaging, and antiviral and anticancer activity. *Nanomedicine* **16**, 1857–1872 (2021)
  22. T. Sun, Y. Yan, Y. Zhao, F. Guo, C. Jiang, Copper oxide nanoparticles induce autophagic cell death in A549 cells. *PLoS ONE* **7**, E43442 (2012)
  23. R. Mohammadinejad, M.A. Moosavi, S. Tavakol, D.Ö. Vardar, A. Hosseini, M. Rahmati, D.J. Klionsky, Necrotic, apoptotic and autophagic cell fates triggered by nanoparticles. *Autophagy* **15**(1), 4–33 (2019)
  24. T. Tanweer, N.F. Rana, I. Saleem, I. Shafique, S.M. Alshahrani, H.A. Almukhlifi, F. Menaa, Dental composites with magnesium doped zinc oxide nanoparticles prevent secondary caries in the alloxan-induced diabetic model. *Int. J. Mol. Sci.* **23**(24), 15926 (2022)
  25. U. Khan, F.A. Jan, R. Ullah, N. Ullah, Comparative photocatalytic performance and therapeutic applications of zinc oxide (ZnO) and neodymium-doped zinc oxide (Nd–ZnO) nanocatalysts against acid yellow-3 dye: kinetic and thermodynamic study of the reaction and effect of various

- parameters. *J. Mater. Sci: Mater. Electron.* (2022). <https://doi.org/10.1007/s10854-021-07483-0>
26. N.M. Almhana, Z.A. Naser, S.Z. Al-Najjar, Z.T. Al-Sharify, T.H. Nail, Photocatalytic degradation of textile dye from wastewater by using ZnS/TiO<sub>2</sub> nanocomposites material. *Egypt. J. Chem.* **65**(13), 481 (2022)
  27. F. Zhao, D. Gao, X. Zhu, Y. Dong, X. Liu, H. Li, Rational design of multifunctional C/N-doped ZnO/Bi<sub>2</sub> WO<sub>6</sub> Z-scheme heterojunction for efficient photocatalytic degradation of antibiotics. *Appl. Surf. Sci.* **587**, 152780 (2022)
  28. A. Serrano-Lázaro, F.A. Verdín-Betancourt, V.K. Jayaraman, A. Hernández-Gordillo, M. de Lourdes López-González, A. Sierra-Santoyo, M. Bizarro, Tracing the degradation pathway of temephos pesticide achieved with photocatalytic ZnO nanostructured films. *Environ. Sci.: Nano* **9**(9), 3538–3550 (2022)
  29. Q.I. Rahman, M. Ahmad, S.K. Misra, M. Lohani, Effective photocatalytic degradation of rhodamine B dye by ZnO nanoparticles. *Mater. Lett.* **91**, 170–174 (2013)
  30. A. Pal, P. Mahamallik, S. Saha, A. Majumdar, Degradation of tetracycline antibiotics by advanced oxidation processes: application of MnO<sub>2</sub> nanomaterials. *Nat. Res. Eng.* **2**, 32–42 (2017)
  31. V. Eskizeybek, F. Sarı, H. Gülce, A. Gülce, A. Avcı, Preparation of the new polyaniline/ZnO nanocomposite and its photocatalytic activity for degradation of methylene blue and malachite green dyes under UV and natural sun lights irradiations. *Appl. Catal. B* **119**, 197–206 (2012)
  32. I. Fatimah, G. Fadillah, I. Yanti, R.A. Doong, Clay-supported metal oxide nanoparticles in catalytic advanced oxidation processes: a review. *Nanomaterials* **12**, 825 (2022)
  33. A.N. Rao, B. Sivasankar, V. Sadasivam, Kinetic studies on the photocatalytic degradation of Direct Yellow 12 in the presence of ZnO catalyst. *J. Mol. Catal. A Chem.* **306**, 77–81 (2009)
  34. V. Etacheri, R. Roshan, V. Kumar, Mg-doped ZnO nanoparticles for efficient sunlight-driven photocatalysis. *ACS Appl. Mater. Interfaces* **4**, 2717–2725 (2012)
  35. S. Suwanboon, P. Amornpitoksuk, P. Bangrak, N. Muensit, Optical, photocatalytic and bactericidal properties of Zn<sub>1-x</sub>LaxO and Zn<sub>1-x</sub>MgxO nanostructures prepared by a sol-gel method. *Ceram. Int.* **5**, 5597–5608 (2013)
  36. W. Shen, Z. Li, H. Wang, Y. Liu, Q. Guo, Y. Zhang, Photocatalytic degradation for methylene blue using zinc oxide prepared by codeposition and sol-gel methods. *J. Hazard. Mater.* **152**, 172–175 (2008)
  37. J. Hu, R.G. Gordon, Deposition of boron doped zinc oxide films and their electrical and optical properties. *J. Electrochem. Soc.* **139**, 2014 (1992)
  38. R.B.H. Tahar, N.B.H. Tahar, Boron-doped zinc oxide thin films prepared by sol-gel technique. *J. Mater. Sci.* **40**, 5285–5289 (2005)
  39. G. Vijayaprasath, R. Murugan, S. Palanisamy, N.M. Prabhu, T. Mahalingam, Y. Hayakawa, G. Ravi, Role of nickel doping on structural, optical, magnetic properties and antibacterial activity of ZnO nanoparticles. *Mater. Res. Bull.* **76**, 48–61 (2016)
  40. X.L. Chen, B.H. Xu, J.M. Xue, Y. Zhao, C.C. Wei, J. Sun, X.H. Geng, Boron-doped zinc oxide thin films for large-area solar cells grown by metal organic chemical vapor deposition. *Thin Solid Films* **515**, 3753–3759 (2007)
  41. S.Y. Lee, W.H. Lan, W.M. Chao, C.W. Tsai, M.C. Shih, Y.D. Wu, Y.T. Hsu, Boron-doped zinc oxide thin films fabricated by ultrasonic spray pyrolysis, In 2012 17th Opto-Electronics and Communications Conference, IEEE, 665–666
  42. V. Vinitha, M. Preeyanghaa, V. Vinesh, R. Dhanalakshmi, B. Neppolian, V. Sivamurugan, Two is better than one: Catalytic, sensing and optical applications of doped zinc oxide nanostructures. *Emerg. Mater.* **4**, 1093–1124 (2021)
  43. L. Yang, Y.P. Zhang, J.W. Xu, H. Wang, Deposition and characterization of boron doped zno thin films by ultrasonic spray pyrolysis method. *Appl. Mech. Mater.* **475**, 1280–1283 (2014)
  44. H.J. Ali, Boron doped zinc oxide for ethanol and CO gas sensing. *MJS* **29**, 150–154 (2018)
  45. S.T. Rattanachan, P. Krongarrom, T. Fangsuwannarak, Boron doping effects on the structural and optical properties of sol-gel transparent ZnO films. *Key Eng. Mater.* **547**, 145–151 (2013)
  46. R.E. Nunez-Salas, A. Hernández-Ramírez, L. Hinojosa-Reyes, J.L. Guzmán-Mar, M. Villanueva-Rodriguez, M. de Lourdes Maya-Trevino, Cyanide degradation in aqueous solution by heterogeneous photocatalysis using boron-doped zinc oxide. *Catal. Today* **328**, 202–209 (2019)
  47. S.D. Senol, O. Ozturk, C. Terzioğlu, Effect of boron doping on the structural, optical and electrical properties of ZnO nanoparticles produced by the hydrothermal method. *Ceram. Int.* **41**, 11194–11201 (2015)
  48. L. Fanni, Explaining Morphological and Electrical Features of Boron-doped Zinc Oxide to Tailor New Electrodes for Photovoltaics. (No. THESIS). EPFL, 2016
  49. A.A. Ahmad, A.M. Alsaad, Q.M. Al-Bataineh, M.A. Al-Naafa, Optical and structural investigations of dip-synthesized boron-doped ZnO-seeded platforms for ZnO nanostructures. *Appl. Phys. A* **124**, 1–13 (2018)
  50. R. Sakthivel, J. Malika, Characterization of Mg doped ZnO nanoparticles synthesized by a novel green route using azadirachta indica gum and its antibacterial activity, *World. J Pharm Pharm Sci.* **6**, 1189–1201 (2017)



51. S.D. Senol, Influence of Mg doping on the structural, optical, and electrical properties of  $Zn_{0.95}Li_{0.05}O$  Nanoparticles. *Int. J. Appl. Ceram. Technol.* **16**, 138–145 (2019)
52. A. Maru, H. Kamble, A. Kalarikkal, R. Shah, P. Bhanuse, N. Pradhan, Mg doped ZnO dilute magnetic oxides prepared by chemical method. *Int. J. Chem. Phys. Sci* **5**, 44–49 (2020)
53. Y.B. Chan, V. Selvanathan, L.H. Tey, M. Akhtaruzzaman, F.H. Anur, S. Djearamane, M. Aminuzzaman, Effect of calcination temperature on structural, morphological and optical properties of copper oxide nanostructures derived from garcinia mangostana L. Leaf Extract. *Nanomater.* **12**(20), 3589 (2022)
54. T. Patra, A. Mohanty, L. Singh, S. Muduli, P.K. Parhi, T.R. Sahoo, Effect of calcination temperature on morphology and phase transformation of MnO<sub>2</sub> nanoparticles: a step toward green synthesis for reactive dye adsorption. *Chemosphere* **288**, 132472 (2022)
55. M.L. Bari, S.H. Sonawane, S. Mishra, T.D. Deshpande, Surfactant assisted reactive crystallization of cobalt oxide nanoparticles in a tubular microreactor: effects of precursor concentrations and type of surfactants. *React. Chem. Eng.* **8**, 355 (2023)
56. Y. Li, Y. Li, A. Xie, Synthesis and optical properties of B-Mg co-doped ZnO nanoparticles. *Coatings* **11**(8), 882 (2021)
57. B. Yalcin, S. Ozcelik, K. Icin, K. Senturk, B. Ozcelik, L. Arda, Structural, optical, magnetic, photocatalytic activity and related biological effects of CoFe<sub>2</sub>O<sub>4</sub> ferrite nanoparticles. *J. Mater. Sci.: Mater. Electron.* **32**, 13068–13080 (2021)
58. J. Kansy, Microcomputer program for analysis of positron annihilation lifetime spectra, *Nucl. Instrum. Methods. Phys. Res. B Nucl. Instrum. Meth. A* **374**, 235–244 (1996)
59. D. Schrader, Compounds of positrons and positronium, principles and applications of positron & positronium. *Chemistry* **17**, 17–36 (2003)
60. U. Yahsi, H. Deligöz, C. Tav, K. Ulutas, D. Deger, S. Yilmazturk, S. Yakut, Ionic conductivity of PVDF-co-HFP/LiClO<sub>4</sub> in terms of free volume defects probed by positron annihilation lifetime spectroscopy. *Radiat. Eff.* **174**, 214–228 (2019)
61. U. Soykan, B.O. Sen, S. Cetin, U. Yahsi, C. Tav, A detailed survey for determination of the grafted semifluorinated acrylic compound effect on thermal, microstructural, free volume, mechanical and morphological features of HDPE. *J. Fluor. Chem.* **233**, 109511 (2020)
62. J.W. Rhim, S. Kuzeci, S. Roy, N. Akti, C. Tav, U. Yahsi, Effect of free volume on curcumin release from various polymer-based composite films analyzed using positron annihilation lifetime spectroscopy. *Materials* **14**, 5679 (2021)
63. Y. Kobayashi, W. Zheng, E.F. Meyer, J.D. McGervey, A.M. Jamieson, R. Simha, Free volume and physical aging of poly (vinyl acetate) studied by positron annihilation. *Macromolecules* **22**, 2302–2306 (1989)
64. Z. Yu, U. Yahsi, J. McGervey, A.M. Jamieson, R. Simha, Molecular weight-dependence of free volume in polystyrene studied by positron annihilation measurements. *J. Polym. Sci. B Polym. Phys.* **32**, 2637–2644 (1994)
65. S.D. Senol, E. Ozugurlu, L. Arda, The effect of cobalt and boron on the structural, microstructural, and optoelectronic properties of ZnO nanoparticles. *Ceram. Int.* **46**, 7033–7044 (2020)
66. B. Yalcin, D. Akcan, I.E. Yalcin, M.C. Alphan, K. Sentürk, I.I. Özyigit, L. Arda, Effect of mg doping on morphology, photocatalytic activity and related biological properties of Zn<sub>1-x</sub>Mg<sub>x</sub>O nanoparticles. *Turk. J. Chem.* **44**, 1177–1199 (2020)
67. A. Guler, L. Arda, N. Dogan, C. Boyraz, E. Ozugurlu, The annealing effect on microstructure and ESR properties of (Cu/Ni) co-doped ZnO nanoparticles. *Ceram. Int.* **45**, 1737–17451 (2019)
68. C. Boyraz, N. Dogan, L. Arda, Microstructure and magnetic behavior of (Mg/Ni) co-doped ZnO nanoparticles. *Ceram. Int.* **43**, 15986–15991 (2017)
69. S.D. Senol, E. Ozugurlu, L. Arda, Synthesis, structure and optical properties of (Mn/Cu) co-doped ZnO nanoparticles. *J. Alloys. Compd.* **822**, 153514 (2020)
70. C. Yu, H. He, X. Liu, J. Zeng, Z. Liu, Novel SiO<sub>2</sub> nanoparticle-decorated BiOCl nanosheets exhibiting high photocatalytic performances for the removal of organic pollutants, *Chinese. J. Catal.* **40**, 1212–1221 (2019)
71. V.K. Mande, D.N. Bhojar, S.K. Vyawahare, K.M. Jadhav, Effect of Zn<sup>2+</sup>–Cr<sup>3+</sup> substitution on structural, morphological, magnetic and electrical properties of NiFe<sub>2</sub>O<sub>4</sub> ferrite nanoparticles. *J. Mater. Sci.:Mater. Electron.* **29**, 15259–15270 (2018)
72. A.A. Dakhel, Structural, optical and electrical measurements on boron-doped CdO thin films. *J. Mater. Sci.* **46**, 6925–6931 (2011)
73. K. Rekha, M. Nirmala, M.G. Nair, A. Anukaliani, Structural, optical, photocatalytic and antibacterial activity of zinc oxide and manganese doped zinc oxide nanoparticles. *Physica B Condens* **405**, 3180–3185 (2010)
74. F. Barra, R. Espinoza-González, H. Fernández, F. Lund, A. Maurel, V. Pagneux, The use of ultrasound to measure dislocation density. *JOM* **67**, 1856–1863 (2015)
75. K.H. Markiewicz, P. Zembko, K. Półtorak, I. Misztalewska, S. Wojtulewski, A.M. Majcher, A.Z. Wilczewska, Magnetic nanoparticles with chelating shells prepared by RAFT/MADIX polymerization. *New J. Chem.* **40**, 9223–9231 (2016)

76. C.L. Hsu, Y.J. Li, H.J. Jian, S.G. Harroun, S.C. Wei, R. Ravindranath, H.T. Chang, Green synthesis of catalytic gold/bismuth oxyiodide nanocomposites with oxygen vacancies for treatment of bacterial infections. *Nanoscale* **10**, 11808–11819 (2018)

**Publisher's Note** Springer Nature remains neutral with regard to jurisdictional claims in published maps and institutional affiliations.

Springer Nature or its licensor (e.g. a society or other partner) holds exclusive rights to this article under a publishing agreement with the author(s) or other rightsholder(s); author self-archiving of the accepted manuscript version of this article is solely governed by the terms of such publishing agreement and applicable law.